Publication No. U-4789
NASA CR 86343

FINAL TECHNICAL REPORT

ATTENUATION MEASUREMENTS IN ARTIFICIAL CLOUDS

By Darrell E. Burch, John D. Pembrook, and Elias Reisman

March 1970

Distribution of this report is provided in the interest of information exchange and should not be construed as endorsement by NASA of the material presented. Responsibility for the contents resides with the organization that prepared it.

Prepared under Contract No. NAS 12-2124
PHILCO-FORD CORPORATION
Aeronutronic Division
Newport Beach, California 92663

Electronics Research Center
NATIONAL AERONAUTICS AND SPACE ADMINISTRATION

Publication No. U-4789
NASA CR 86343

FINAL TECHNICAL REPORT

ATTENUATION MEASUREMENTS IN ARTIFICIAL CLOUDS

By Darrell E. Burch, John D. Pembrook, and Elias Reisman

March 1970

Prepared under Contract No. NAS 12-2124
PHILCO-FORD CORPORATION
Aeronutronic Division
Newport Beach, California 92663

Electronics Research Center
NATIONAL AERONAUTICS AND SPACE ADMINISTRATION

TABLE OF CONTENTS

LIST OF FIGURES AND TABLES

LIST OF FIGURES AND TABLES (Cont.)

LIST OF FIGURES AND TABLES (Cont.)

FINAL TECHNICAL REPORT
ATTENUATION MEASUREMENTS IN ARTIFICIAL CLOUDS

By Darrell E. Burch, John D. Pembrook, and Elias Reisman

Philco-Ford Corporation
Aeronutronic Division
Newport Beach, California 92663

SUMMARY

A CO_2 laser operating at 10.6 μ and an He-Ne laser at 0.6328 μ have been used as radiation sources to study the attenuation and near-forward scattering of artificial fogs. Scattering angles varied from 10 to 40 milliradians. Both water fogs and ice fogs have been used. The experimental results compare favorably with calculated values based on Mie theory, both in the amount of scattered power and in its angular dependence. From these results, we conclude that Mie theory, which is based on spherical particles, can be applied to scattering by ice particles in the near-forward directions. Mie theory, however, may break down for larger ice particles, and almost certainly will not apply for scattering at larger angles.

The extinction of both ice fogs and water fogs has been measured at several wavelengths between 2.3 and 3.6 μ. This region is of interest because of the occurrence of wide variations in the real and imaginary components of the index of refraction. A narrow "window" occurs at approximately 2.75 μ for water clouds and near 2.83 μ for ice clouds. The shapes of spectral curves of transmittance or of the extinction cross-section depend strongly on the particle-size distribution. Our results indicate that significant errors exist in the published index of refraction values for ice near 2.8 μ. Simultaneous measurements of attenuation or scattering at two different wavelengths provide information on particle-size distribution, influence of irregular shapes, and index of refraction which cannot be obtained from single-wavelength measurements.

SECTION 1

INTRODUCTION

Although scattering of electromagnetic radiation by fogs and clouds has been a subject of study for several years, most of the work has been confined to the visible portion of the spectrum. Only a limited amount of work has been done in the infrared. During the past several years interest in the infrared transmission and scattering by clouds has increased because of the advent of numerous infrared communications systems and increased activity in fields related to atmospheric radiation transfer. The invention of the CO_2 laser and its potential use in communications has stimulated interest in the scattering properties of fogs and clouds in the 10 μ region.

Among the first to make extensive infrared measurements on the attenuation by natural fogs was Arnulf et al (Ref. 1). These workers confined their work to atmospheric windows and found that the transmittance of haze increases markedly with increasing wavelength from the visible to 10 μ. This increase was not found for fogs which consist of larger particles than the haze. Farmer (Ref. 2) has also measured cloud attenuation from the visible to 5.5 μ and has found that the clouds become increasingly transparent as the wavelength is increased. Differences in particle-size distribution may account for the difference in the wavelength dependences observed by these two groups.

Blau et al (Refs. 3, 4) have investigated the back-scattering and attenuation by natural clouds with an airborne instrument. Most of their results could be explained, at least qualitatively, on the basis of existing cloud models and Mie scattering theory. However, these workers observed a "window" in cirrus clouds near 2.85 μ where the attenuation is significantly less than at nearby wavelengths. This unexpected phenomenon has led to the laboratory work discussed in Section 4.

Most of the limited amount of scattering work done in the infrared has involved only the attenuation. Insufficient experimental results on the scattering functions are available in the infrared to provide checks on the validity of cloud models, Mie theory, and the published values of the indices of refraction. Mie theory has been shown to be applicable in the visible for water droplets which are spherical and have negligible absorption (i.e., the imaginary part of the index is very small). Comparisons need to be made between calculated scattering functions and experimental measurements at infrared wavelengths where absorption plays an important role. In some spectral regions, there is considerable uncertainty in the published values of the complex index of refraction, which is a required input for Mie theory computations. Direct measurement of the real and imaginary parts of the index of refraction is difficult, particularly in regions where n_i is very large. Therefore, an alternative approach is to measure attenuation or scattering in special regions of interest and to compare the results with calculated values.

The general objective of the present program has been to make relatively simple measurements designed to check the validity of Mie theory under several special conditions and to investigate any anomalies that might be observed. Artificial fogs generated in the laboratory were to be used because of several advantages they have over natural fogs and clouds for certain types of measurements. Artificial fogs can be partially controlled and repeated so that measurements made at different times can be compared. Of course, the instrumentation required in the laboratory is much simpler, and because of the shorter atmospheric path, the absorption by H_2O, CO_2 and other atmospheric gases is reduced greatly. A technique for generating artificial water fogs had already been developed and used in our laboratory by Reisman et al (Ref. 5) and by Johnston and Burch (Ref. 6). These workers found that the particle-size distribution of the artificial water fogs is apparently similar to that found in natural fogs by Arnulf et al (Ref. 1). Johnston and Burch compared the attenuation in the visible to that at a few wavelengths in infrared windows. Generally, there was good agreement between the experimental and theoretical results.

In early 1969, personnel from our laboratory started a small-scale company-sponsored project involving attenuation by natural clouds. The sun serves as a radiation source and is tracked by a coelostat. The attenuation by a cloud is determined by comparing the radiation received when the sky is clear with that received when the cloud is in the line-of-sight. At first, measurements were made at 0.63 μ and at one other wavelength isolated and detected by a prism spectrometer. Later, the instrument was modified to monitor simultaneously the radiation at 0.63 μ, 10.6 μ, and a third wavelength, usually between 8 and 13 μ. This arrangement made it possible to determine the relative attenuation of the same cloud at various wavelengths and to compare the results with predictions based on Mie scattering theory and existing cloud models. The important parameter for a cloud model is the particle-size distribution function. Deirmendjian (Refs. 7, 8) has derived particle-size distribution functions for a variety of clouds.

The results of this experiment for water clouds confirm previous work. Ratios of the attenuation coefficients at various wavelengths are similar to calculations based on Deirmendjian's cloud models. They are also in general agreement with the work done in our laboratory on artificial water fogs by Johnston and Burch (Ref. 6). One somewhat surprising result was obtained for cirrus clouds composed of ice particles. The ratio of the apparent attenuation coefficient at 10.6 μ to that at 0.63 μ is always greater than unity. Typically, the ratio is between 1.3 and 1.4, but for some clouds it has been as high as 1.6. By comparison, this ratio for water clouds varies from 0.25 to 0.5, depending on the type of cloud and its stage of development or dissipation. It was generally believed that cloud attenuation would be less near 10 μ than in the visible.

Since the sun is not a point source but subtends a finite solid angle, some radiation scattered in the near-forward direction may be detected. This is particularly true at 0.63 μ since more scattered radiation is directed in the near-forward direction for short wavelengths than for long wavelengths. Therefore, the apparent ratio of the attenuation at 10.6 μ to that at 0.63 μ may be increased by forward-scattered radiation which is detected. Nevertheless, the large ratio observed for ice clouds seemed to need further investigation since the physics is not well understood and the 10.6 μ region is of special interest to communications engineers.

Because of the surprising results on ice clouds, we decided to give detailed measurements of the attenuation by artificial ice clouds at 0.63 μ and 10.6 μ the highest priority among the projects in the present investigation. We have built a chamber in which ice clouds can be produced and the characteristics are moderately reproducible. An He-Ne laser operating at 0.6328 μ and a CO_2 laser at 10.6 μ have been used as sources to measure the attenuation and scattering in the near-forward direction. The detectors have been calibrated so that absolute measurements of the scattered radiation could be made. Water fogs generated by the technique described by Reisman et al (Ref. 5) have also been investigated in the same manner.

We have used a Mie theory computer program to calculate the absolute scattering functions for both wavelengths studied. Values of the real and imaginary indices of refraction used in the calculation are from Irvine and Pollack (Ref. 9). The size distribution of the water fogs is reasonably well known from the previous work by Reisman et al. Different size distributions have been used for the artificial ice fogs. Generally speaking, the agreement between our calculated and experimental results is quite good, probably within experimental error. Therefore, we conclude that Mie theory is probably adequate at these wavelengths for the attenuation and near-forward scattering calculations. The irregular shapes of ice crystals may cause a breakdown of Mie theory at larger scattering angles, or for larger particles. Ice particles in natural clouds are probably larger than those in our artificial ice clouds. The large particles in natural clouds are probably the major factor contributing to the large attenuation observed at 10.6 μ.

The results of the 0.6328 μ and 10.6 μ measurements are discussed in Section 3 along with some rather peculiar phenomena related to the growth of ice particles. Since the results of the work on attenuation of solar radiation by natural clouds is closely related to the present work, we have included a discussion of these results in Appendix A.

Blau et al (Refs. 3, 4) have not been able to account for the window they observed in cirrus clouds on the basis of published values of the complex index of refraction. The window is at a wavelength where n_r, the real part of the index of refraction for ice, is low, and where n_i, the imaginary part is increasing rapidly with increasing wavelength. The importance of a possible window in clouds is obvious, and further investigation is more than justified. Therefore, as a part of the present study, we have investigated the attenuation of artificial ice clouds in this spectral region (2.3-3.6 μ) under controlled laboratory conditions. Since curves of n_i and n_r, as tabulated by Irvine and Pollack, for water are similar to those for ice, we might expect a window to occur in water fogs as well. Therefore, we also explored artificial water clouds in the same spectral region.

Section 4 describes the results of this investigation. We have observed the narrow window discovered by Blau in ice clouds, although it is only about 0.1 micron wide and not particularly transparent. The extinction coefficient of our ice clouds is slightly less than half as much at the center of the window as at neighboring wavelengths.

We have found that a similar window exists for water fogs and that the shape of the transmittance curve, or of a curve of extinction coefficients, depends very strongly on particle sizes. Using Mie theory with Irvine and Pollack's indices of refraction for water, we can show that the window disappears for very small (radius $r < 0.1$ μ) or large ($r > 10$ μ) particles. A similar dependence on particle size is to be expected for ice clouds.

Aside from the importance of the window, the investigation in the 2.3-3.6 μ region has been quite informative. Transmittance measurements were made at 2.45 μ, and the results of these measurements served as a reference while the transmittance simultaneously was measured at other wavelengths. Since the difference between the two wavelengths was small, the difference in size parameter ($x = 2\pi r/\lambda$) was small, thus the variations in transmittance were due to differences in n_i and n_r. The influence of large values of n_i has been demonstrated; for particles of small radius, r, the extinction increases with n_i and is nearly independent of n_r. For large particles ($r \gg \lambda$), the extinction is nearly independent of both n_i and n_r. Calculations made with our Mie theory computer program and a series of articles by Plass (Ref. 10) and by Kattawar and Plass (Refs. 11, 12) have been used extensively in interpreting our experimental results.

SECTION 2

FOG GENERATION

Water Fog Generation

There are two fundamental techniques for generating water fogs. In the mechanical or uniphase method, droplets are created from bulk water by nozzles, impellers, or centrifuge discs. In the thermodynamic or duophase method, droplets are created from vapor-saturated air by varying one or more of the thermodynamic parameters such as pressure or temperature. Since the thermodynamic techniques are responsible for naturally-occurring fogs and clouds, their use in creating artificial fogs gives rise to particle-size distributions similar to those occurring naturally. The mechanical techniques are used primarily to create fogs throughout extensive volumes for extended periods of time.

We chose a thermodynamic technique that had been employed successfully in earlier scattering experiments at Aeronutronic by Reisman, Cumming, and Bartky (Ref. 5). The fog is generated in a series of wooden chambers, 60 cm square and 120 cm long, which can be coupled together to form a tunnel of convenient length. In the forward-scattering experiments discussed in Section 3, only two sections were used in order to ensure the unobstructed exit of forward-scattered energy. This 240 cm path also was used for the attenuation measurements discussed in Section 4. Each chamber is equipped with heated water trays in the base and cooling coils at the top. Liquid nitrogen serves as the coolant.

A reliable and repeatable fog can be obtained by establishing a cycle wherein the air is first saturated by heating the water in the trays, then subsequently chilled to create a fog which eventually dissipates, restoring the chamber to its starting condition. The cycle is then repeated. During the cycle the temperatures of the water in the trays, the chamber air, and the room air are monitored. In the present study the air temperature in the chamber has been cycled between 21.7°C and 16°C with the room at approximately 23°C. A full cycle requires about 30 minutes. The scattering measurements are generally made during a 10 minute portion of the cycle while the fog dissipates. By relating the scattering to its corresponding transmission condition, we have been able to obtain consistent and repeatable results for any number of independent experiments, provided the cycle is maintained. Representative plots of the transmittance of the fog versus time are presented in Section 4, along with discussion of the particle-size distribution.

Ice Fog Generation

A pure ice fog is not as simple to obtain as a pure water fog because of a metastable condition which can be created wherein the fog persists as super-cooled water droplets at temperatures as low as -40°C. The addition of ice nucleation centers such as AgI to a super-cooled fog chamber upsets the metastable conditions and causes ice crystals to grow at the expense of the water and vapor content of the chamber. Ice crystals have been grown at temperatures as high as -4°C using AgI. Below -40°C, the nucleation of ice crystals occurs spontaneously, and it is generally agreed that the super-cooled state does not exist below this temperature. Between 0°C and -40°C, it is possible to have a super-cooled water fog, or ice fog, or, in a dynamic system, a combination of both. In order to ensure that the principal source of scattering would be ice crystals, we have performed most of the experiments at chamber temperature sufficiently far below -40°C that we could rely on spontaneous nucleation. (For a discussion of ice fogs and ice clouds, see Mason (Ref. 13).)

The ice fogs have been generated in a chamber specificially designed for this purpose. The chamber, which is shown in Figure 2-1, consists of a double-walled cylinder 213 cm long with an inner diameter of 46 cm and an outer diameter of 56 cm. The inner and outer walls of the cylinder form a tank which is filled with a solution of ethylene glycol and water. The solution is cooled by flowing liquid nitrogen through copper coils immersed in it. A motor-driven paddle wheel stirs the solution and ensures a uniform temperature at the chamber wall. The sides of the tank are insulated with foamed plastic approximately 10 cm thick. Plywood sheets protect the foam insulation and held it in place as it was poured, in liquid form, around the chamber and allowed to solidify. The open ends of the chamber are covered with 10 cm thick styrofoam plates. The walls of the inner cylinder and the end plates thus constitute a cold box in which the fogs are grown. Thermocouples monitor the temperatures of the wall and several points in the air along the beam. The primary beams traverse the chamber along the axis of the cylinder through openings cut in the end plates. In the scattering experiments, the opening in the exit end of the chamber is sufficiently large to permit the exit of light scattered at angles as great as 44 milliradians from the primary beam.

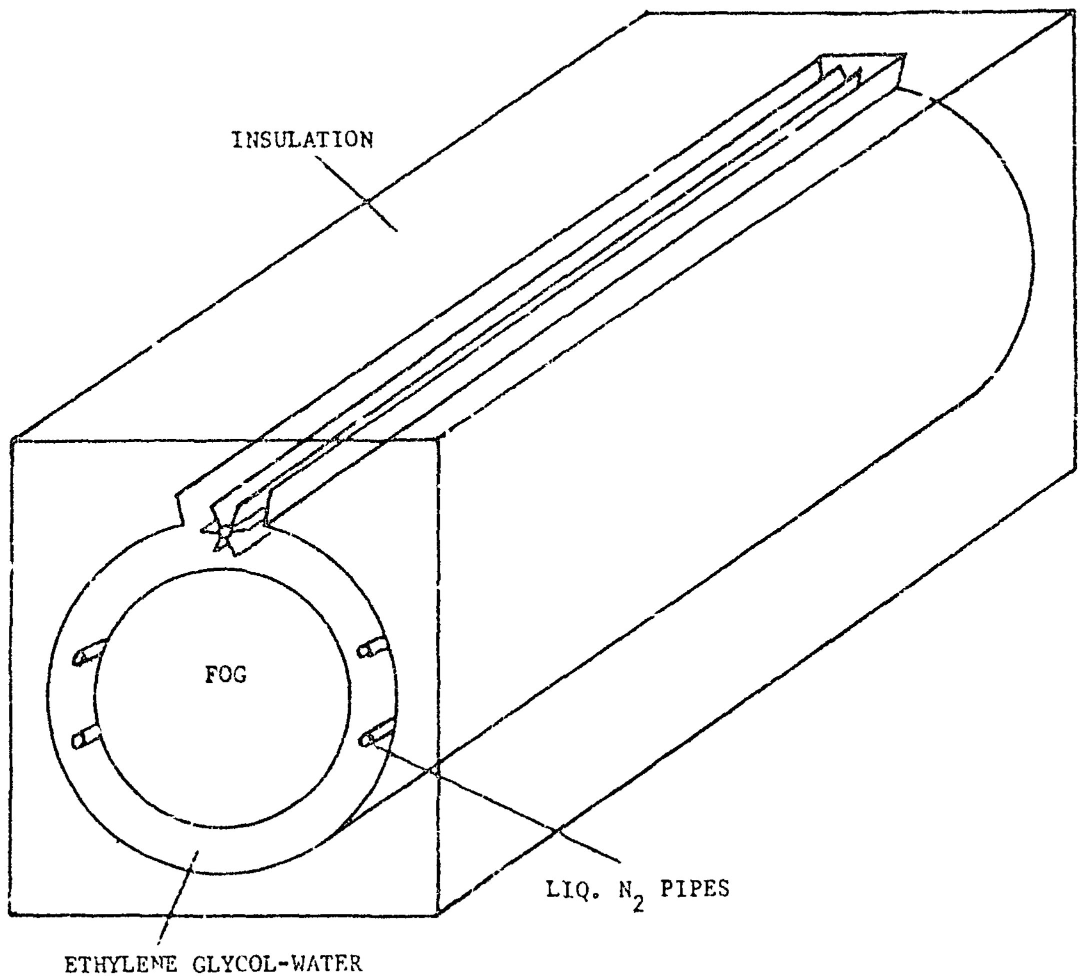

FIG. 2-1. Chamber used to generate ice fogs.

Two techniques have been used to study the behavior of the ice fogs: In the first method, the chamber is sealed before the start of the experiment. After the chamber has been sealed for several minutes, the plugs in the end plates are removed, and the transmittance and/or scattered radiant energy is monitored as the fog evolves. When the ice fog reaches a quasi-steady state, the end plates are replugged and the chamber environment is permitted to return to its initial state. The procedure is then repeated for a new angle or new wavelength after the internal air temperature cools to within about 2°C of the inside wall. The air temperature rises approximately 2°C more while the chamber is open. In the second method, the chamber is left open and allowed to reach a quasi-steady state condition while several measurements may be made. In both methods the wall temperatures are maintained near -52°C. For the quasi-steady state experiment, the air temperature rises about 10°C above the wall temperature.

When the chamber is first unplugged, there is usually a slight residual ice fog which appears to almost dissipate in about 30 or 45 seconds. The particles then grow, and after about 1 to 1.5 minutes, the fog reaches maximum density. The transmittance then slowly increases until after 3 to 5 minutes the quasi-steady state is established. Representative plots of the transmittance versus time are presented in Section 4. Plots of the extinction cross-section ratio at two wavelengths and the angular scattering cross-sections versus time are shown in Section 3. An analysis of the growth process of the particles is given in Section 3.

SECTION 3

TRANSMISSION AND NEAR-FORWARD SCATTERING AT 0.6328 AND 10.6 MICRONS

Optical Arrangement

A schematic diagram of the optical arrangement used to measure transmission and near-forward scattering at 0.6328 and 10.6 μ is shown in Fig. 3-1. The upper portion of the figure shows the transmitting optics, and the lower portion shows the apparatus which collects and detects the energy after it has passed through a fog chamber. A 50 milliwatt beam at 0.6328 μ from a He-Ne laser is combined with a 10 watt beam at 10.6 μ from a CO_2 laser by a germanium flat. The flat transmits the 10.6 μ beam and is placed in it at Brewster's angle so that there is negligible reflection. The 0.6328 μ beam is reflected from the flat at the emergent point of the 10.6 μ energy. Having the beam coincident within the fog chamber facilitates alignment of the optical components and eliminates variation in the fog between the two beams.

A polished chopper (C) operating at 720 hertz serves three purposes. First, it chops the beam so that a phase-locked amplifier can be used. Second, it reflects almost specularly the 10.6μ beam onto a thermopile TP(1) which continuously monitors the power. Finally, the chopper diffusely reflects a portion of the 0.6328 μ energy onto a photomultiplier tube PM(1). The output of this tube provides the reference signal for a phase-locked amplifier. Narrow band-pass interference filters on all the photomultiplier tubes reduce the ambient radiation.

Mirrors M1 and M2 expand the dual wavelength beam from a nominal diameter of 4 mm to approximately 5.6 cm. Three aperture stops clean up and define the beam. The first stop, just after the 10.6 μ laser, removes peripheral radiation. The second stop blocks energy scattered

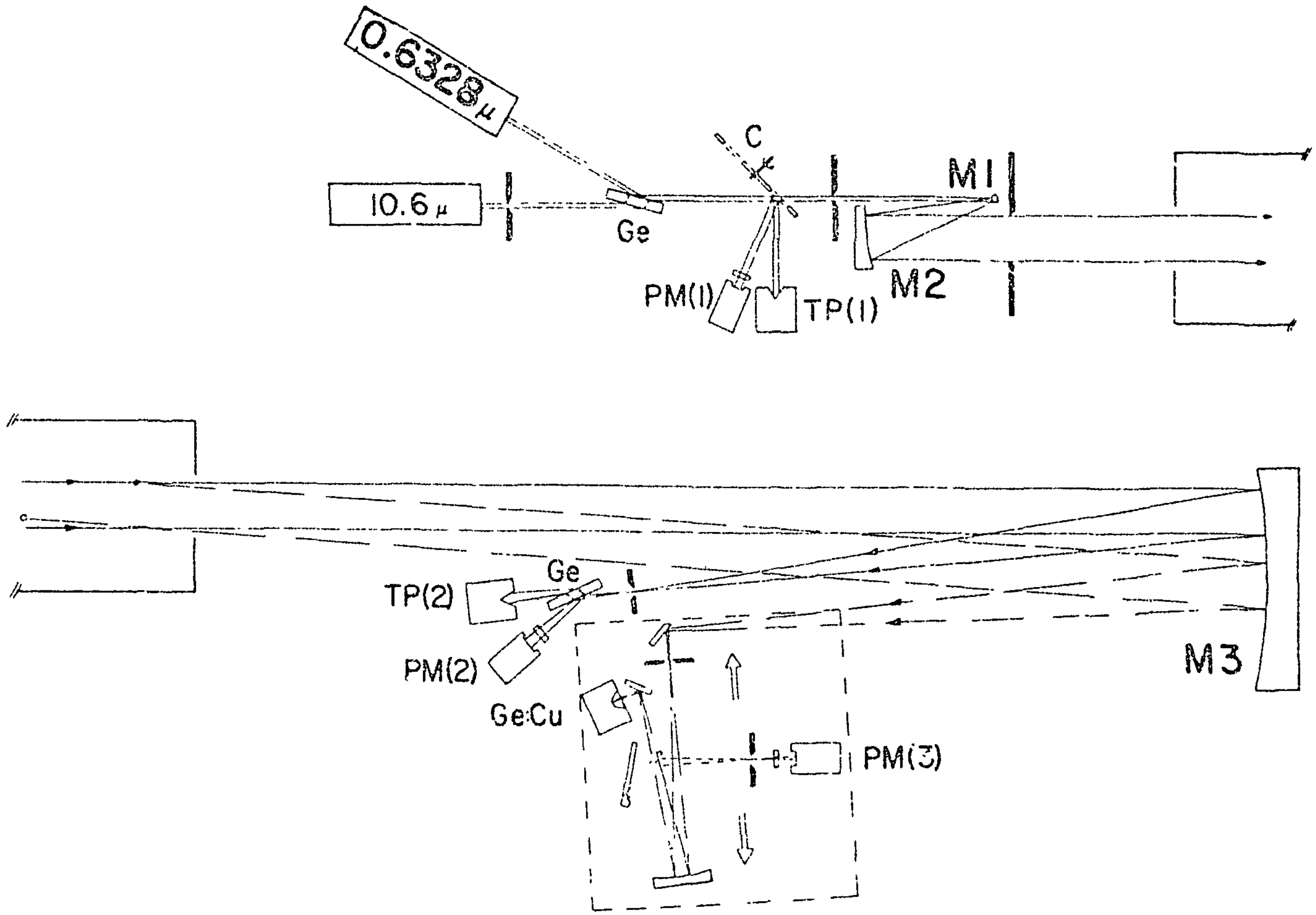

FIG. 3-1. Optical Arrangements for Transmission and Near-Forward Scattering Measurements

from imperfections in the Ge flat, peripheral light from the 0.6328 μ laser beam, and part of the energy diffracted by the edge of the chopper. The third stop, which limits the size of the beam, is square with 4 cm sides oriented 45° from the vertical. This shape and orientation minimizes the diffracted energy in the horizontal plane where the near-forward scattering is measured. This size removes most of the energy scattered from the optical surfaces while still transmitting nearly all of the primary beam.

The energy transmitted through the fog in the chamber and that scattered by it in the near-forward direction are collected by mirror M3 which is placed sufficiently close to the chamber to collect single-scattered energy between zero and 44 milliradians. Scattering data are obtained between 5 and 40 milliradians.

The unscattered, transmitted energy is separated into two beams by a second Ge flat set of Brewster's angle. The transmitted 10.6 μ power is monitored by thermopile TP(2). The transmitted, 0.6328 μ beam is reflected by the Ge flat and is monitored by a photomultiplier tube PM(2). A field stop placed at the focal point of M3 subtends about 5 milliradians and is the entrance aperture to a box enclosing the transmission monitor system. The stop prevents some of the energy scattered at very small angles from entering the transmission monitors. The box precludes energy scattered from the Ge flat and the two detectors from being detected as background by the scattering detectors.

The assembly used to measure near-forward scattering is mounted on a sliding carriage which makes measurements possible at any angle between 2 and 44 milliradians. A flat mirror placed just ahead of the focal plane of mirror M3 folds the focal plane to a field stop which is parallel to the axis of M3. One edge of the flat mirror is beveled so that the reflecting surface can be located close to the primary beam without disturbing it. As the flat mirror and stop move with the sliding carriage, the stop effectively moves across the focal plane providing an angular scan of the scattered energy. Throughout this experiment the stop was adjusted to subtend 2 milliradians.

When measuring the scattered power at 10.6 μ, a spherical mirror forms an image of the field stop on the sensitive element of a helium-cooled Ge:Cu detector. The diameter of the sensitive element is approximately 50 percent greater than the diameter of the stop image so that vignetting caused by mirror alignment errors is avoided. A flat mirror rotated into the beam directs it through a stop at the image plane to a photomultiplier tube PM(3) which measures the scattered 0.6328 μ power. The stop diameter in front of PM(3) is the same as the Ge:Cu element.

The outputs of the two thermopiles and the photomultiplier PM(2) are recorded directly by strip chart recorders. The output of the Ge:Cu detector or of PM(3), whichever is in the beam, is amplified by a lock-in amplifier and displayed on a strip chart recorder.

The background power is almost negligible when measuring near-forward scattering at 0.6328 μ. For example, in a small-particle ice fog, the signal-to-background ratio is about 10, 30, 60, and 250 at 5, 10, 15, and 20 milliradians, respectively. At 10.6 μ, however, the scattering coefficients of the fog are considerably smaller than at 0.6328 μ, and the background power is quite significant. For a similar ice fog the signal-to-background ratios at 10.6 μ are only about 1.3, 4.7, 9, 20, 60, and 70 at 5, 10, 15, 20, 30, and 40 milliradians, respectively. For such a fog, data obtained at less than 15 milliradians are used only to check for gross changes of the scattered power.

At 10.6 μ the ratio of the background power measured with no fog to the primary beam power is approximately 6×10^{-6}, 1×10^{-6}, 1×10^{-7}, 5×10^{-8}, and 4×10^{-8} at 5, 10, 20, 30, and 40 milliradians, respectively. The above examples of signal-to-background ratios are for the least dense ice fogs consisting of the smallest particles considered usable. For fogs which are more dense or contain larger particles, the signal-to-background ratio is more favorable.

Symbols and Terminology

The transmittance is given by

$$T = I/I_o = \exp(-\gamma z), \tag{3-1}$$

where I_o is the initial intensity of a beam and I is the intensity after the beam has propagated a distance z through the fog. In the following discussion we assume that I includes only the unattenuated portion of the original beam; it does not include any forward-scattered energy. The extinction coefficient γ can be thought of as the sum of an absorption coefficient a and a scattering coefficient b. Consider a unit volume containing N particles of radius r. The amount of light scattered by the volume of unit length Δz is given by

$$\Delta I = I_o N \pi r^2 Q_{sca} \Delta z, \tag{3-2}$$

where Q_{sca} is a dimensionless quantity called the scattering efficiency and is a function of r and wavelength λ. The quantity $\pi r^2 Q_{sca}$ is called the scattering cross-section of the particle and is symbolized by σ_{sca}.

The quantity Q_{sca} is defined as the ratio of the scattering cross-section to the geometric cross-section (πr^2). Thus

$$b = N \pi r^2 Q_{sca} = N \sigma_{sca}(r). \tag{3-3}$$

When the particles are not of the same size, b is obtained by summing over a distribution.

$$b = \sum_r N_r \pi r^2 Q_{sca}(r) \tag{3-4}$$

where N_r is the number of particles of radius r per unit volume. Normally, the sum is replaced by an integral:

$$b = \int N(r) \pi r^2 Q_{sca}(r) dr = \int N(r) \sigma_{sca}(r) dr, \tag{3-5}$$

where N(r)dr is the number of particles in the unit volume with sizes between r and r + dr. Furthermore, the size distribution function N(r)dr frequently is normalized and treated as the probability function p(r), such that

$$p(r)dr = \frac{N(r)dr}{\int N(r)dr} = \frac{N(r)dr}{N_o}, \tag{3-6}$$

and finally,

$$b = N_o \int p(r) \sigma_{sca}(r) dr = N_o \sigma_{sca}, \tag{3-7}$$

where N_o is the number of particles per unit volume and σ_{sca} is the average cross-section per particle.

The quantity σ_{sca} which has the dimension of area, may be treated as the integral of an angular scattering distribution function, $\sigma(\theta)$, such that

$$\sigma_{sca} = \int \sigma(\theta) d\Omega, \tag{3-8}$$

where Ω is the solid angle in steradians.

If the radiation is polarized, the expression is more complicated:

$$\sigma_{sca} = \int \left[\sigma_{\perp}(\theta) \cos^2 \varphi + \sigma_{\parallel}(\theta) \sin^2 \varphi\right] d\Omega, \tag{3-9}$$

where $\sigma_{\perp}(\theta)$ is the angular scattering distribution function for light polarized perpendicular to the scattering plane, $\sigma_{//}(\theta)$ is the angular scattering distribution function for light polarized in the scattering plane, and φ is taken as zero in the scattering plane. Since σ_{sca} cannot depend on the polarization state of the incident light, it follows that:

$$\sigma(\theta) = \frac{\sigma_{\perp}(\theta) + \sigma_{//}(\theta)}{2}. \tag{3-10}$$

A consideration of the absorption coefficient a gives rise to terms analogous to those defined in scattering. Thus, there are $Q_{abs}(r)$, the absorption efficiency, and $\sigma_{abs}(r)$, the absorption cross-section. The equation corresponding to Eq. (3-7) reads:

$$a = N_o \sigma_{abs} \tag{3-11}$$

and

$$\gamma = N_o \sigma_{sca} + N_o \sigma_{abs} = N_o \sigma_{ext}. \tag{3-12}$$

The appropriate form for the particle-size distribution function is naturally important to any experimental or analytical study. A distribution function possessing the general form:

$$N(r) = r^A \exp(-Br) \tag{3-13}$$

has been used successfully by Deirmendjian (Ref. 8) and Zuev, et al (Ref. 14). It has also been used to fit prior experimental work done in the fog chamber (Reisman et al (Ref. 5)). The peak of this distribution occurs where r = A/B.

Results for Water Fogs

The transmission data were processed first since they are required for the processing of the scattering data. A smooth curve is drawn through the raw data and a series of points tabulated from the smoothed curve. Since the fog chamber completely clears at the end of a run, the 100% transmittance reference is always available. In the case of the CO_2 laser, fluctuations of its power level make it necessary to reconstruct the 100% transmittance reference from the monitor trace. Because the visible transmission covers such a wide dynamic range, it is always necessary to change recorder scales during the run. It is convenient to replot the data on semi-log paper to recover information occurring at the time of a scale change. A typical time history of the transmission at 0.6328 μ during the portion of the cycle used for data analysis is shown in Fig. 3-2.

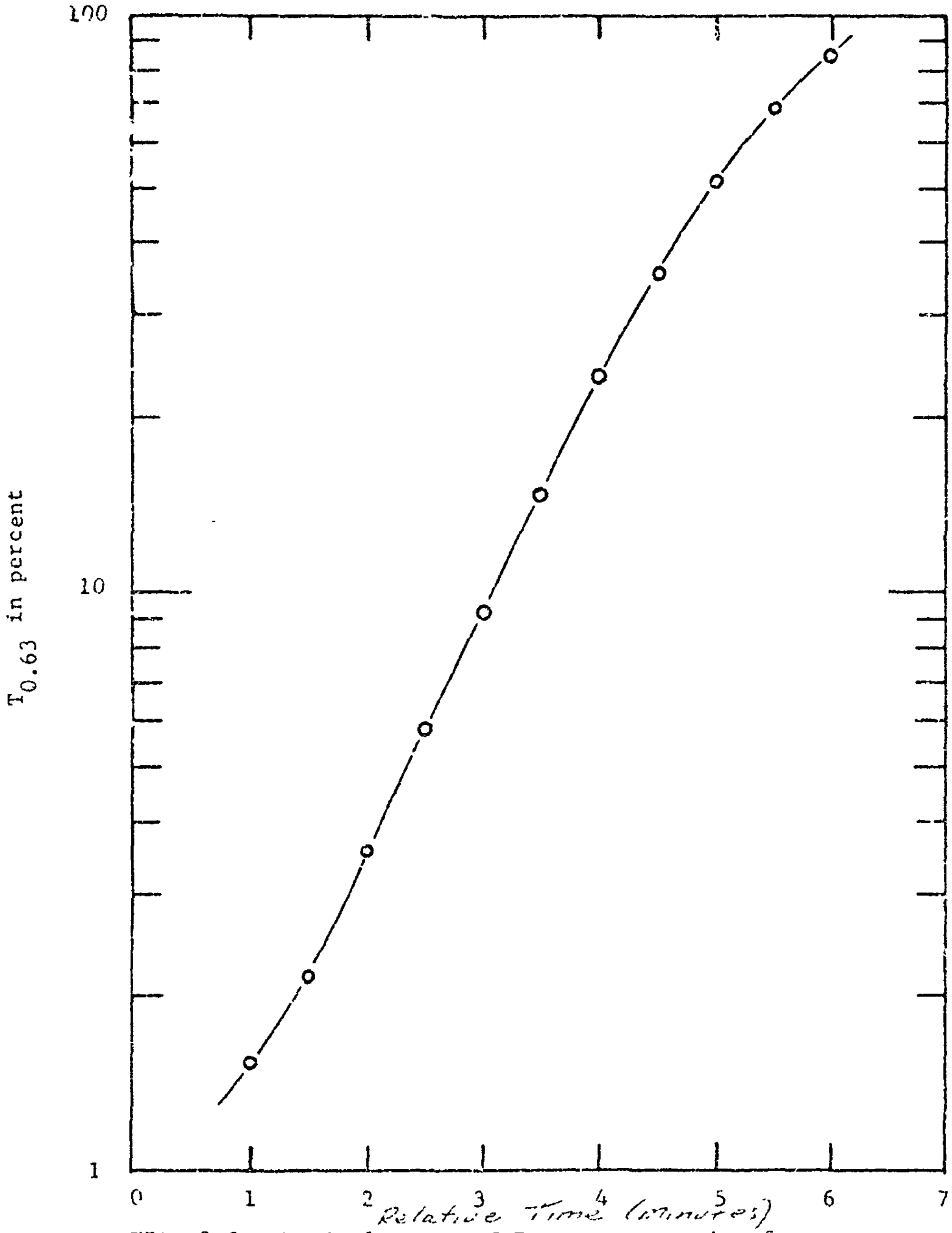

FIG. 3-2. Typical curve of $T_{0.63}$ versus time for a water fog. Zero time corresponds approximately to the time in the cycle when the fog has been generated and is starting to dissipate. The path length is 240 cm.

The change in transmission is due primarily to change in the number of fog particles per unit volume, although there is also a change in the particle-size distribution as subsequent analysis will show. The path length for all the water fog runs was 240 cm.

Transmission data are generally more reliable than scattering data since the former do not require absolute calibration. With very large scattering coefficients, one possible source of error in transmission measurements arises from scattered light entering the transmission monitor. Repeated checks during the course of the experiment showed this did not occur. Varying the aperture immediately preceding the monitors TP(2) and PM(2) produced no significant change. Further, the magnitude of the measured scattered radiation for the solid angle subtended by the transmission monitor was found to be less than the resolution of the instrument.

From Equations (3-1) and (3-12), it follows that

$$\frac{-\ln T_{10.6}}{-\ln T_{0.63}} = \frac{\gamma_{10.6}}{\gamma_{0.63}} = \frac{\sigma_{ext,\ 10.6}}{\sigma_{ext,\ 0.63}} \tag{3-14}$$

where

$$\gamma_\lambda = (-\ln T_\lambda)/L = N_o\, \sigma_{ext,\lambda}.$$

In order to simplify the notation $\sigma_{ext,10.6}/\sigma_{ext,0.63}$ is written as $\sigma_{10.6}/\sigma_{0.63}$. This quantity is plotted as a function of $\gamma_{0.63}$ in Fig. 3-3 for seven independent fog runs. The chamber length L is 240 cm. It is readily apparent that over a wide dynamic range of fog density ($0.0025 \leq \gamma_{0.63} \leq 0.016$) the data points are well superimposed, indicating repeatability. Further, in more than half of the region the function is essentially constant, indicating that the distribution is constant. As the fog dissipates there is a noticeable reduction in $\sigma_{10.6}/\sigma_{0.63}$ which suggests that the particle-size distribution shifts toward smaller particles. Superimposed on the experimental data are the values for $\sigma_{10.6}/\sigma_{0.63}$ calculated for several narrow, square distributions and a particle-size distribution of the $r^A e^{-Br}$ form which has been synthesized to best fit the observed experimental data. The "square" particle-size distributions referred to here and later indicate a distribution with $N(r) = 1$ for $r_o \leq r \leq r_n$ and $N(r) = 0$ for $r < r_o$ or $r > r_m$. The distribution width is usually set at either $2r_o$ or 1 micron, depending upon the purpose of the calculation. The indices of refraction used in this calculation were taken from Irvine and Pollack (Ref. 9). They are $n_r = 1.33$ at 0.6328, and $n_r = 1.178$ and $n_i = 0.075$ at 10.6 μ. n_i was given as 1.1×10^{-8} at 0.6328 μ by Irvine and Pollack but was set equal to zero for computational purposes since its contribution would

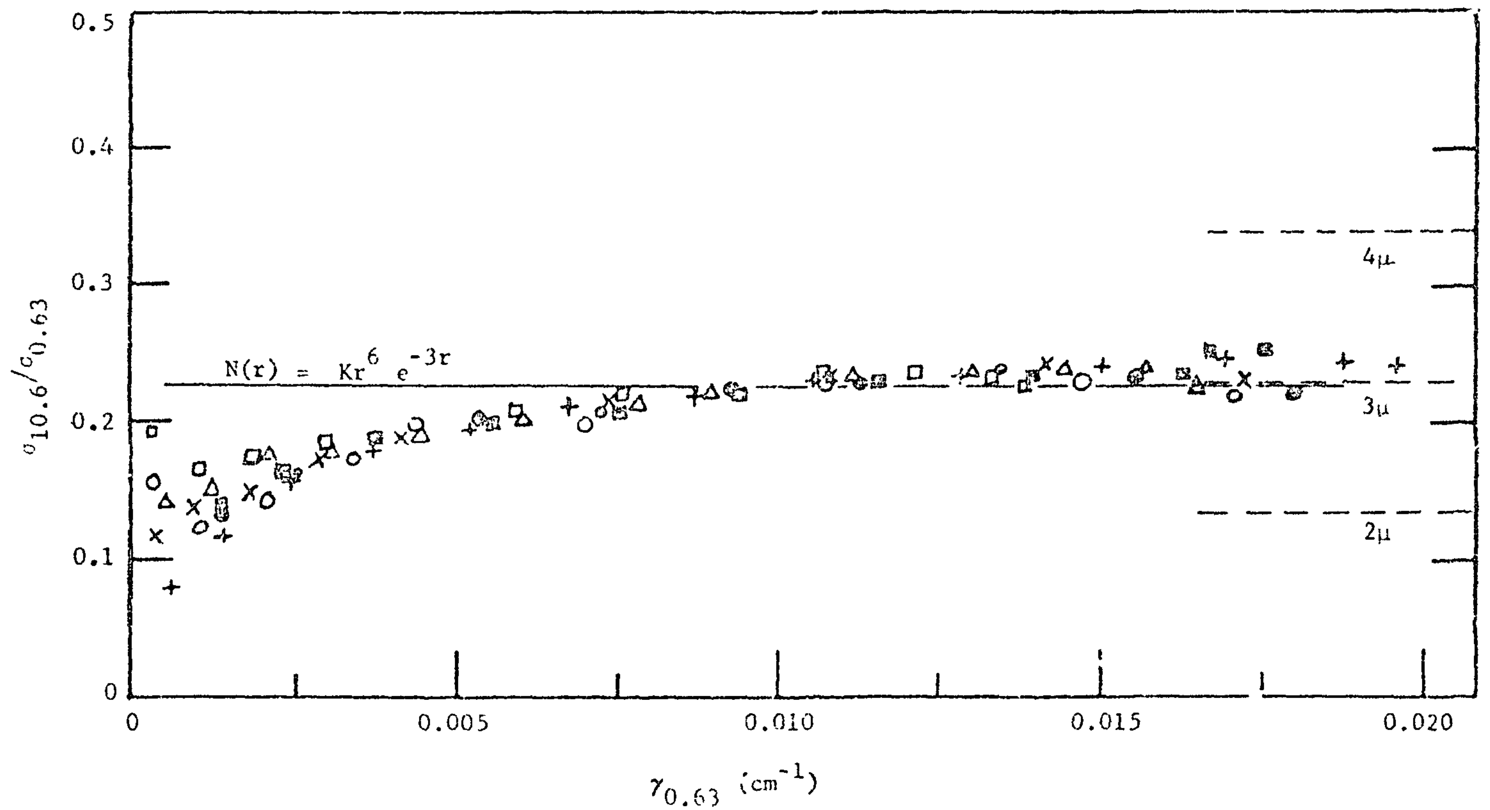

FIG. 3-3. Ratio of extinction cross-sections at 10.6 μ to 0.6328 μ for water fogs versus $\gamma_{0.63}$. The various symbols represent different independent runs. The dashed lines represent calculated values for one micron wide square distributions centered at the indicated radii. N(r) is constant for particle radii within these distributions and zero elsewhere. The solid line represents the calculated value for the Kr^6e^{-3r} distribution which peaks at 2 μ. The index values used in the calculations are: $n_r = 1.33$ and $n_i = 0$ at 0.6328 u; $n_r = 1.178$ and $n_i = 0.075$ at 10.6 μ.

be negligible for the particle sizes considered. A significant savings in computer time was realized by this approximation.

A technique that is currently under investigation in an IR&D program at Philco-Ford involves synthesizing total distributions by using narrow, square distributions. These sub-distributions are assigned various weighting factors and their influence on key scattering parameters are assessed using a slide rule or desk calculator. The technique makes it possible to consider the effect of subtle distribution changes rapidly and inexpensively and to gain insight into the relative sensitivity of an observable to such changes. A more detailed description of the technique and some of the results should be available in mid-1970.

Before comparing the experimental transmission results with the calculations, it is best to consider the experimental scattering results. Unlike the transmission data, the scattering data requires an absolute calibration. This is done by introducing the total primary beam, suitably attenuated, into the appropriate scattering monitor. Then after determination of the attenuation factor, the scattered radiation is treated as a certain fraction of the primary beam since the geometric factors are all known. Possible errors lie in the determination of the attenuation factor. In the case of radiation at 0.6328 μ, Wratten filters were used. Since several were required, the error in density may have approached 0.2, although we feel it is considerably less (i.e., a calibration error of 60%). In the case of the 10.6 μ radiation, the attenuators were Ge flats used as polarizers. These were calibrated by using the power meter and adjusting the power of the laser. Because the dynamic range required reading almost within the noise of the power meter, a possible error of a factor of two is not unreasonable.

In processing the data, corrections are made for the attenuation of the beam before it reaches the scattering volume and again for the attenuation suffered by the scattered beam before it exits from the chamber. We assume that only single-scattered radiation reaches the detector. Consider the power reaching the detector through a small, solid angle $\Delta\Omega$ at an angle θ from a unit scattering volume of length dz which lies a distance z into the chamber of length L. The intensity I incident on the scattering volume is $I_o \exp(-\gamma z)$. The beam intensity scattered toward the detector $\Delta I(\theta)$ is $I N_o \sigma(\theta) \Delta\Omega dz$. This is further attenuated by the remaining chamber length (L-z) and the beam intensity $\Delta I_s(\theta)$ at the detector is $\Delta I(\theta) \exp[-\gamma(L-z)]$. The power reaching the detector from the entire chamber is then:

$$I_s(\theta) = \int_o^L I_o \exp(-\gamma z) N_o \sigma(\theta) \exp[-\gamma(L-z)] \Delta\Omega dz =$$

$$I_o N_o \exp(-\gamma L) \sigma(\theta) \Delta\Omega L = I_o L T N_o \sigma(\theta) \Delta\Omega . \tag{3-15}$$

Note that the contribution of any scattering element to $I_s(\theta)$ is independent of its location within the chamber.

If the particle-size distribution is constant as N_o varies, $\sigma(\theta)$ is also constant and $N_o\,\sigma_{ext}\,L$ is equal to $-\ln T$. It follows that

$$\frac{I_s(\theta)}{I_o\,T} = \frac{\sigma(\theta)}{\sigma_{ext}}\,\Delta\Omega\,(-\ln T), \text{ and } \frac{\sigma(\theta)}{\sigma_{ext}} = \frac{I_s(\theta)}{I_o T \Delta\Omega\,(-\ln T)} \tag{3-16}$$

A typical curve showing the scattering behavior at one angle as a function of $\gamma_{0.63}$ is given in Fig. 3-4. If the distribution were constant, the data would fall on a straight line with a slope of unity. The slope of 1.45 implies either a slight change in particle-size distribution or the presence of multiply-scattered light.

A more graphic picture of the scattering data is shown in Fig. 3-5. The points were obtained from the raw data at several times during a run by the use of Eq. (3-16). The 0.6328 μ data will integrate to unity over a full sphere since $\sigma_{ext} = \sigma_{sca}$ at 0.6328 μ. The data at 10.6 μ will integrate to a value less than unity since $\sigma_{ext} = \sigma_{sca} + \sigma_{abs}$. The quantity σ_{ext} was used in both cases since it is the directly measured variable. Superimposed on the experimental data are corresponding quantities calculated from Mie scattering theory for several narrow, square distributions as well as the "best" synthesized distribution [$N(r) = Kr^6e^{-3r}$]. The near-forward scattering at 10.6 μ is essentially constant over the observed angular interval and, hence, is shown pictorially at 20 and 40 milliradians only. The points have been "fanned" about these angles for better visualization since they overlap each other. The average decrease in value from 0 to 50 milliradians for the four calculated curves at 10.6 μ is only 4.5×10^{-4} ster^{-1}. The near-forward scattering data at 0.6328 μ correlates well with angle and has been plotted at each observation angle. Undoubtedly, the analytical data could be made to fit the experimental points a little better by making subtle changes in the shape of the particle-size distribution function. There is little point in doing this to high precision because of the possible calibration errors discussed earlier. The particle-size distribution used in the calculation is shown in Fig. 3-6. The constants A and B of r^Ae^{-Br} were derived by fitting the curve through three, one-micron wide, square distributions centered at 2, 4, and 6 microns radius. The three square probes had been weighted to best fit the observed data. The curves are normalized to unit area in the calculations; however, the curve illustrated in Fig. 3-6 has been normalized to a peak height of unity for illustrative purposes. The distribution is quite similar to that observed experimentally by Arnulf (Ref. 1) in his numerous measurements of the particle sizes in natural fogs. The complete angular scattering distribution function for water for this particle distribution is shown in Fig. 3-7.

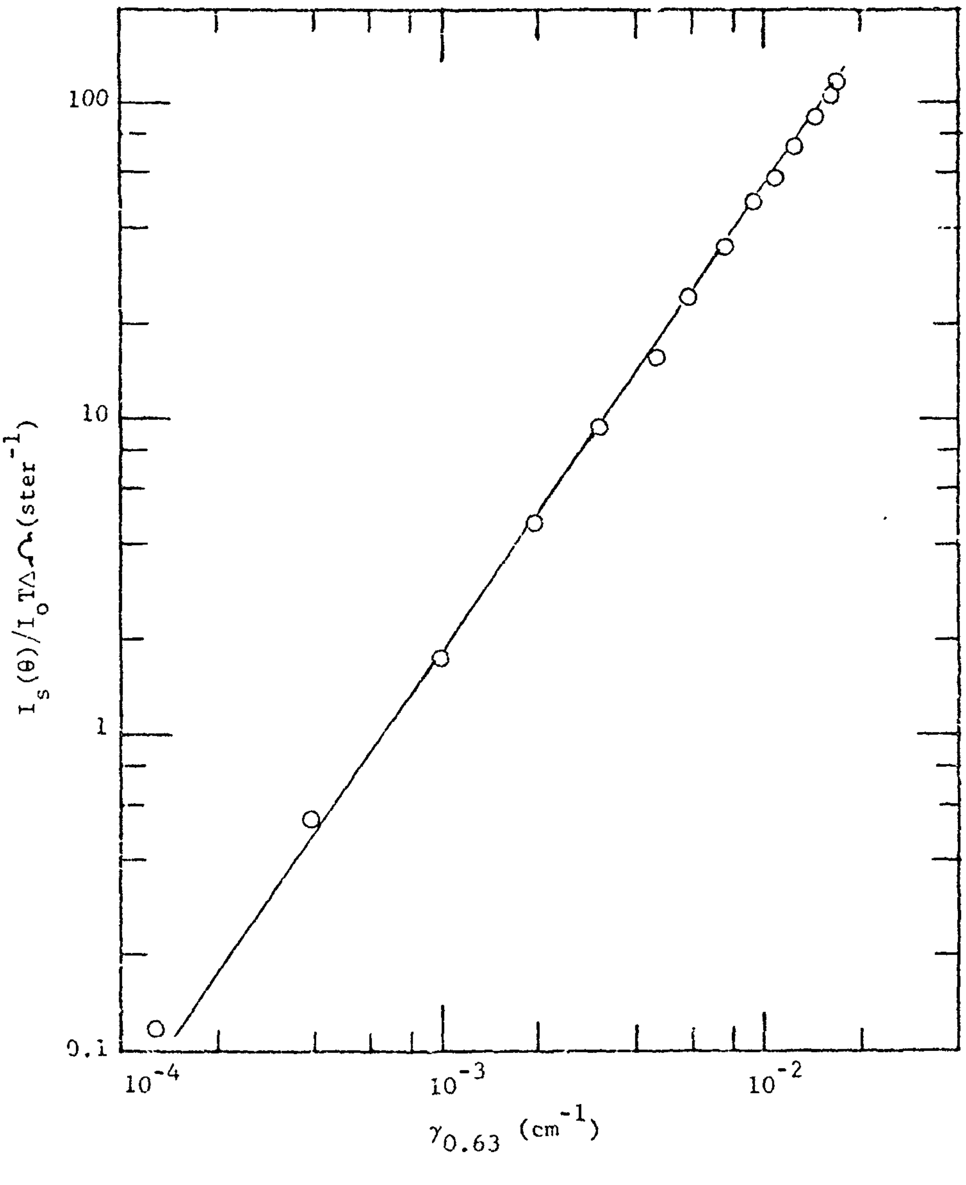

FIG. 3-4. Ratio of scattered power at 30 milliradians to the product $I_o\ T\Delta\Omega$ versus $\gamma_{0.63}$. The wavelength is 0.6328 μ.

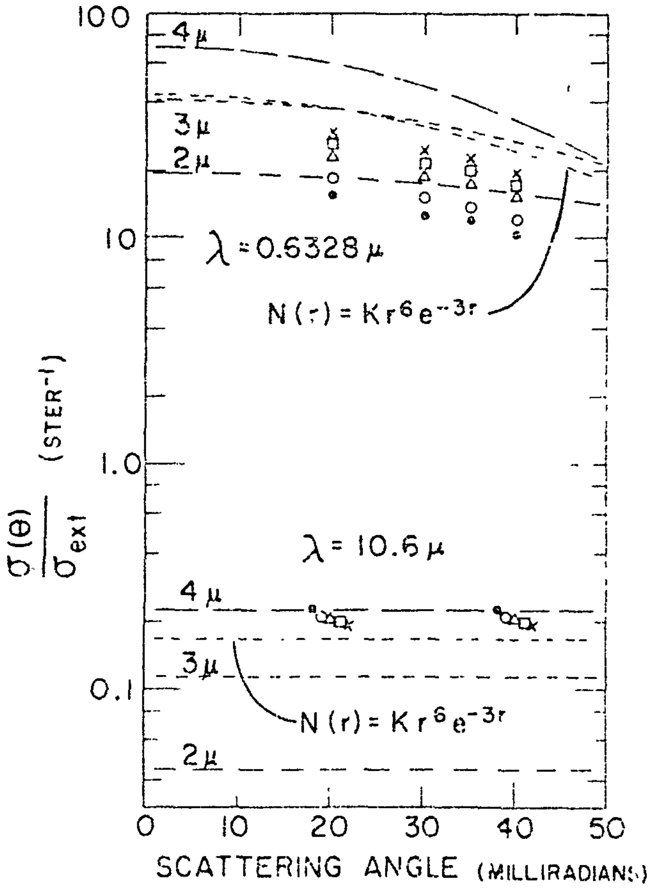

FIG. 3-5. Angular plot of normalized scattering data at 0.6328 μ and 10.6 μ wavelength and calculated curves for various particle-size distributions. The index values used in the calculations are: $n_r = 1.33$ and $n_i = 0$ at 0.6328 μ; $n_r = 1.178$ and $n_i = 0.075$ at 10.6 μ. Except for the Kr^6e^{-3r} distribution, the calculated curves are for 1 μ wide square distributions centered at the indicated radii. The 0.6328 μ parameters corresponding to the experimental points are:

Point	$\gamma_{0.63}$	$-\ln T_{0.63}$	$T_{0.63}$
X	0.0125 cm^{-1}	3.00	0.05
□	0.0096 cm^{-1}	2.30	0.10
△	0.00705 cm^{-1}	1.69	0.184
○	0.00417 cm^{-1}	1.00	0.368
⊙	0.00288 cm^{-1}	0.69	0.50

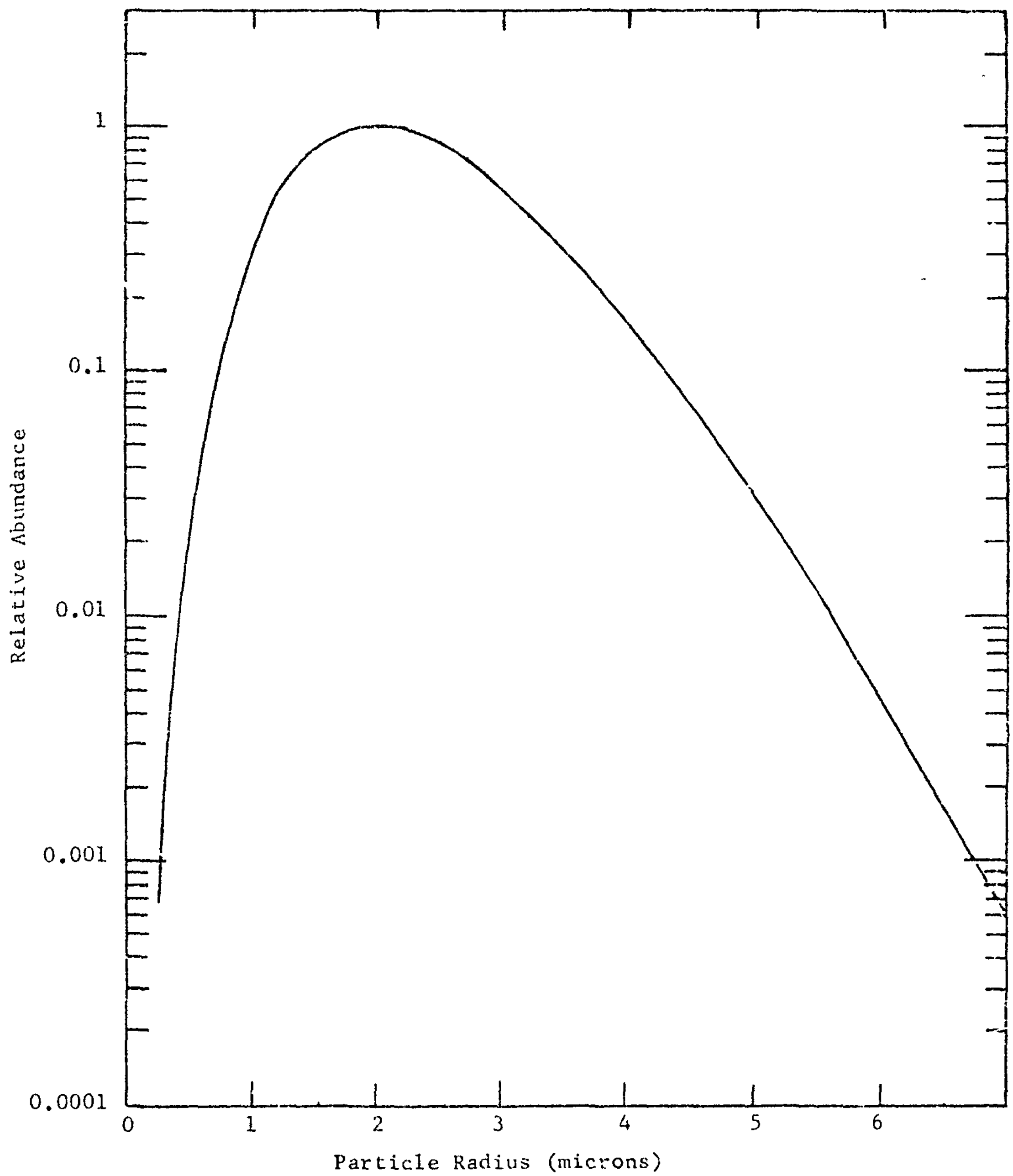

FIG. 3-6. Particle-size distribution function. The ordinate is $r^6 e^{-3r/2^6} e^{-6}$.

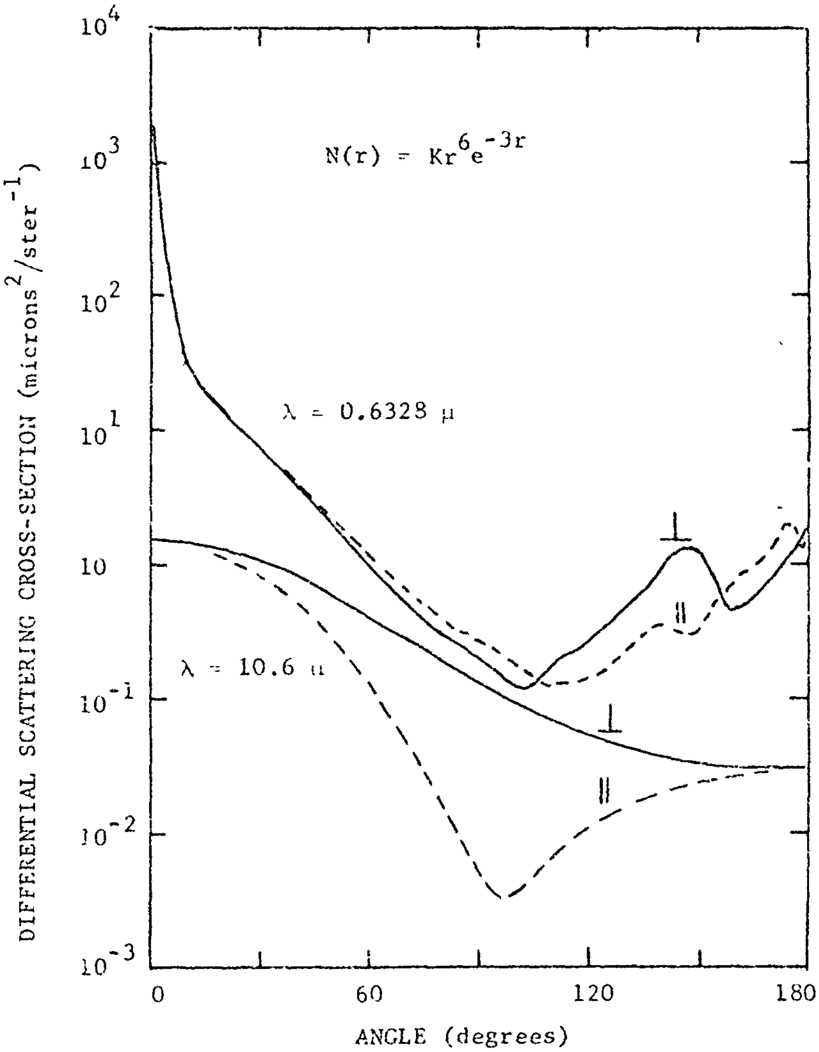

FIG. 3-7. Angular plots of the differential scattering cross-section for water. The parallel and perpendicular components are shown for the indicated wavelengths and particle-size distribution. The index values used are: $n_r = 1.33$ and $n_i = 0$ at $0.6328\ \mu$; $n_r = 1.178$ and $n_i = 0.075$ at $10.6\ \mu$.

There are distinct differences in the behavior of the scattering data at the two wavelengths. One of the most obvious differences is that the normalized scattering at 10.6 μ appears to be very insensitive to changes in fog density. This could mean that $\sigma(\theta)/\sigma_{ext}$ is insensitive to changes in the particle-size distribution associated with changing density. However, the analytical behavior as judged by the square distributions readily disproves this assumption. The only reasonable conclusion is that the distribution undergoes only minor changes during the observation time and has a form which minimizes the influence of these changes on $\sigma(\theta)/\sigma_{ext}$ at 10.6 μ. The value of $\sigma(\theta)/\sigma_{ext}$ at 0.6328 μ behaves differently. As the fog evolves there is a monotonic decrease in the normalized scattering. It is important to note, however, that the shape of the function does not change (i.e., the slope) as might be predicted from the behavior of the scattering functions calculated from the square distributions. In fact, in fitting the data to an analytical distribution, the shape influenced the selection more than the absolute value. Thus the 2 μ square distribution was not considered seriously although the scattering value matched well. If there is minimal absorption, the detector can record radiation which has been scattered multiply and, hence, it records a higher value than single scattering alone predicts. This may account for some of the spread in data at 0.6328 μ. Furthermore, the added component would be very insensitive to angle since it arises from an integral over all angles. The net result would be curves that decrease monotonically with decreasing fog density and maintain their shapes (i.e., slopes). A detailed analysis of the multiple scattering is beyond the scope of this program.

It is clear from the large dynamic ranges covered by the extinction and scattering coefficients during an experiment, that N_o or σ_{ext} or both are changing with time. A plot of $\sigma_{10.6}/\sigma_{0.63}$ shows no great change over a wide range of $N_o\ \sigma_{0.63}$, i.e., $\gamma_{0.63}$, which strongly suggests that most of the effect is due to a changing N_o. Figure 3-3 taken by itself and analyzed only with square distribution functions (i.e., in this case $\pm$0.5 μ from nominal) implies a nearly constant size distribution of 3 μ for the dense fog (i.e., $\gamma_{0.63}$ between 0.010 and 0.017 cm^{-1}) and then a slightly decreasing average radius for less-dense fogs.

The normalized scattering function ($\sigma(\theta)/\sigma_{ext}$) at 10.6 μ appears to be constant for a wide range of $\gamma_{0.63}$. It is fit with a 4 μ square distribution function in Fig. 3-5. This fit may be deceptive since the uncertainty in the calibration could be a factor of 2. Thus a 3 μ square distribution might also fit. In either case, it doesn't show the spread that might be expected from the $\sigma_{10.6}/\sigma_{0.63}$ curves. The 0.6328 μ scattering data fit a 3 μ square distribution function quite well insofar as slope is concerned, but misses badly in absolute value, probably beyond the possible error. Since we have assumed that the shifts in the 0.6328 μ scattering curves are caused by multiple scattering and not by distribution changes which cause a change in slope, we must fit the experimental data of the lightest fog (i.e., least multiple scattering) to the theoretical curve. The distribution $N(r) = Kr^6e^{-3r}$ appears to fit the data well, except for the magnitude of the visible scattering. It also is a better fit of the measured angular scattering distribution function (Ref. 5) and the particle-size distribution measured by Arnulf (Ref. 1) in natural fogs. At small angles $\sigma(\theta)$ increases more rapidly than σ_{ext} with increasing particle size. Therefore, $\sigma(\theta)/\sigma_{ext}$ increases with particle size and a few large particles in the tail of a size distribution strongly influence the observed and calculated values of $\sigma(\theta)/\sigma_{ext}$. Thus, caution must be used in comparing the experimental data with the values calculated from square probe distributions. This is clearly shown by examining Figures 3-3, 3-5, and 3-6. The distribution shown in Fig. 3-6 peaks at 2 μ. At 3 μ, N(r) has decreased by a factor of 1.8 and at 4 μ N(2)/N(4) is 6.1. Yet due to the rapid increase in σ with radius, the value of $\sigma_{10.6}/\sigma_{0.63}$ shown in Fig. 3-3 for the r^6e^{-3r} distribution is almost identical to the value for the 3 μ square distribution. Figure 3-5 shows the same results at 0.6328 μ for $\sigma(\theta)/\sigma_{ext}$. At 10.6 μ in Fig. 3-5 the effect is even more pronounced and $\sigma(\theta)/\sigma_{ext}$ for the r^6e^{-3r} distribution falls between the values computed for the 3 and 4 μ square distributions.

The one inconsistency that all of these measurements leave is the answer to the question of how the distribution changes as the fog evolves. On the basis of extinction ratios, the size decreases as the fog evolves. The near-forward scattering data imply that the size remains constant. Finally, large angle scattering data (Ref. 5) indicate increasing sizes. Since the size changes are small, the particle-size distribution is probably changing in a way that is not adequately described by a single size parameter. The combined effects of condensation or evaporation, agglomeration and fall out might, for example, increase the size of the peak while lowering the number of particles in the tail. In the right combination such a change might account for all the effects.

Some comments should be made relating the fogs in the experiment to fogs as they naturally occur. One of the facts which make comparison difficult is the extremely diverse size distributions which are reported in the literature. Since the particle number density is often determined by normalizing to the total mass of liquid water of density ρ in a unit volume,

$$m = \int N_o\, p(r)\, \frac{4\pi r^3}{3}\, \rho\, dr,$$

the value of N_o is even more diverse than the shape of the distribution. Accurate collection of drop samples is exceedingly difficult since the smaller droplets invariably follow the air stream and miss the collector. Ranz and Wong (Ref. 15) have made a careful parametric study of the problem and have calculated collection efficiencies for a variety of types and shapes of collectors. Careful experiments like those performed by Arnulf (Ref. 1), in which he uses 0.01 μ spider webs to collect his samples, always yield distributions which peak well below 10 μ radius. In particular, Arnulf's curves all peak at about 2 μ radius. Experiments of the 1930's and 1940's indicated peaks around 40 μ; apparently few of the smaller particles were collected. Once a distribution has been assumed and the corresponding σ has been calculated, the extinction coefficient easily can be related to number density. For the $N(r) = Kr^6e^{-3r}$ distribution, which peaks at $r = 2$ μ, $\sigma_{0.63}$ is approximately 43×10^{-8} cm^2. If N_o is 1000 particles per cm^3, $\gamma_{0.63}$ is about 40 km^{-1}, which corresponds to a dense fog. The extinction coefficient for the artificial fogs in this experiment ranged from 200 to 1600 km^{-1} (i.e., 4000 - 32,000 particles/cm^3).

Results for Ice Fogs

The diagnostics for the ice fog experiments were identical to those used for the water fogs. The transmittances at 0.6328 μ and 10.6 μ were monitored along with the output of the CO_2 laser. The fourth monitor again recorded the radiation scattered at the selected angle and wavelength. Two techniques of ice fog generation were used. These are described in an earlier section. The first of these techniques, wherein the chamber is sealed between experiments, was given primary emphasis. The other technique was not as satisfactory since the temperature of the chamber changed considerably from experiment to experiment while the end plugs were open. The discussion which follows will pertain almost entirely to the first technique and will amplify some of the descriptions in the section on fog generation.

When the chamber is unplugged an evolutionary process begins which is about the same from run to run. At first there is a slight residual ice fog which appears to almost clear up after several seconds. The transmittance at both 0.6328 μ and 10.6 μ reaches some initial value within two or three seconds after the plug is removed and then slowly increases for about 10 seconds. During the next 40 seconds the particles increase in number and grow, and the fog rapidly increases in density. For the next minute the fog density slowly decreases and finally reaches an equilibrium. The particles can be seen scintillating, and the most notable ones may be as large as 10 to 15 μ in radius, judging from the free fall rate (i.e., about 2.5 cm/sec). However, since the ice particles are not spherical, the size may be underestimated. In any event, this probably represents an upper limit to be associated with the tail of some size distribution.

The behavior of the ice fog up to the point of maximum extinction can vary from run to run, possibly because it is difficult to create precisely the same initial conditions, such as temperature, humidity, number of seed particles, etc., each time. Once the fog is dense, it appears much more repeatable. The data were taken from the charts beginning slightly before the transmittance minimum and proceeding at fixed intervals of 15 seconds. The data taken from each of the charts were tabulated, and a computer was used to calculate the values of key functions such as $\sigma_{10.6}/\sigma_{0.63}$. This quantity is plotted in Fig. 3-8 versus the extinction coefficient, $\gamma_{0.63}$, which is related to the transmittance, chamber length L(210 cm), N_o, and σ_{ext} by:

$$\gamma = (-\ln T)/L = N_o \sigma_{ext}.$$

During a single run, γ decreases by only a limited amount from its maximum value to a point where steady state is reached. However, on succeeding runs the chamber proceeds to warm up and successive data points are shifted to lower values of γ. During run 103, for example, the chamber wall temperature was about -52°C. Run 128 was made with the wall at about -50°C. Figure 3-8 shows $\Delta\gamma_{0.63}$ to vary from about 0.003 cm^{-1} to about 0.007 cm^{-1} with a mean of 0.0045 cm^{-1} over the data portion of the six runs shown. This spread in $\gamma_{0.63}$ per run and between runs is typical of all the ice data. Note that $\sigma_{10.6}/\sigma_{0.63}$ increases slightly with decreasing $\gamma_{0.63}$. This implies a growth in the mean particle size during each run and between successive runs.

Although the simple Mie theory is not completely applicable to non-spherical particles, it can be used to estimate average cross-sections and forward-scattering, particularly for larger particles where the forward-scattering arises from diffraction around the edges of the particles. Calculated values of $\sigma_{10.6}/\sigma_{0.63}$ for several square particle distributions also are shown in Fig. 3-8. The indices used for the calculation at [illegible] μ are from Irvine and Pollack (Ref. 9); however, their tables do not [illegible] wavelengths < 0.95 μ for ice. Thus, we set the index values for λ [illegible] to those for water at 0.6328 μ since they are similar in the visib[illegible].

Figure 3-9 shows the normalized scattering $\sigma(\theta)/\sigma_{ext}$ plotted as a function of angle in the near-forward direction for both wavelengths. The functions are plotted for several values of extinction coefficient. The points were obtained by selecting a small range of extinction and finding the value of the normalized scattering function at a given angle. When two or more data points on a given run could be used, or where two runs overlapped, $\sigma(\theta)/\sigma_{ext}$ was obtained by averaging. Also included in Fig. 3-9 are the curves of $\sigma(\theta)/\sigma_{ext}$ calculated for several square distributions. $\sigma(\theta)/\sigma_{ext}$ is almost independent of angle at 10.6 μ for small angles. The decrease in value from 0 to 50 milliradians for the calculated curves at 10.6 μ varies from 4.5×10^{-4} to 59×10^{-4} $ster^{-1}$ as the mean radii increase from 3 to 6 μ. The change in $\gamma_{0.63}$ between runs does not allow overlap of the data for all the $\gamma_{0.63}$ values selected for presentation in Fig. 3-9. Therefore, the number of $\sigma(\theta)/\sigma_{ext}$ versus angle and $\gamma_{0.63}$ points vary as a function of the time sequence in which the runs were made.

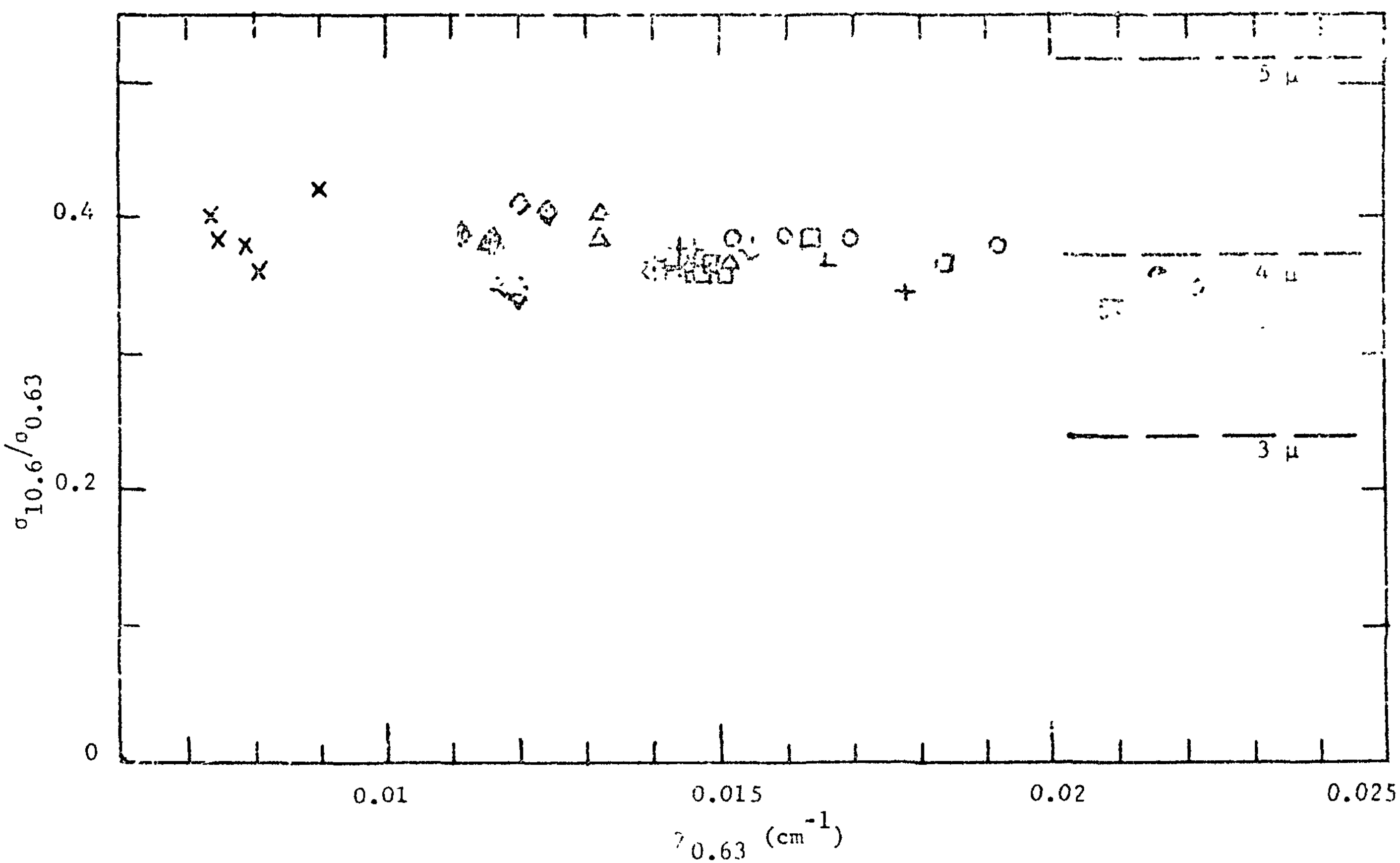

FIG. 3-8. Extinction cross-section ratios at 10.6 μ to 0.6328 μ for several ice fogs versus $\gamma_{0.63}$. The various symbols represent different independent runs. The dashed lines represent calculated values for one micron wide square distributions centered at the indicated radii. The index values used in the calculations are: $n_r = 1.33$ and $n_i = 0$ at 0.6328 μ; $n_r = 1.213$ and $n_i = 0.0655$ at 10.6 μ.

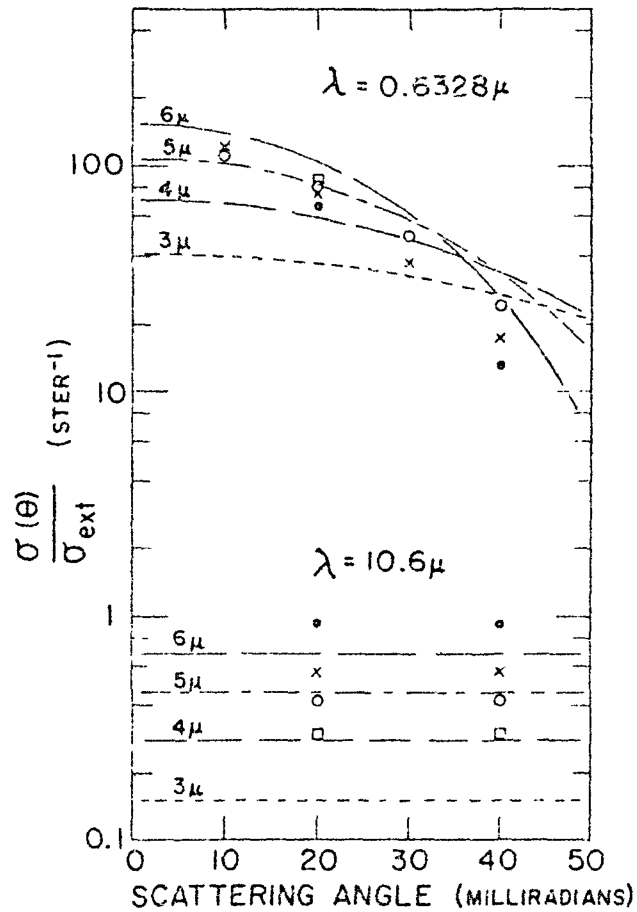

FIG. 3-9. Angular plot of normalized scattering data at 0.6328 μ and 10.6 μ wavelength and calculated curves for various particle-size distributions. The index values used in the calculations are: $n_r = 1.33$ and $n_i = 0$ at 0.6328 μ; $n_r = 1.213$ and $n_i = 0.1555$ at 10.6 μ. The calculated curves are for 1 μ wide square distributions centered at the indicated radii. The 0.6328 μ parameters corresponding to the experimental points are:

Point	$\gamma_{0.63}$	$-\ln T_{0.63}$	$T_{0.63}$
□	0.018 cm^{-1}	3.84	0.022
O	0.015 cm^{-1}	3.20	0.041
X	0.012 cm^{-1}	2.56	0.077
⊕	0.008 cm^{-1}	1.70	0.182

The ice fog particles as judged from $\sigma_{10.6}/\sigma_{0.63}$ seem to grow slightly during a run (as $N_o \sigma_{ext}$ decreases). They also seem to grow from run to run as again $N_o \sigma_{ext}$ decreases and the chamber wall temperature increases. This implies that N_o is decreasing and that particle sizes are increasing. The equivalent square distribution radius which best fits the data is centered at about 4 μ. It seems probable that the peak of the true distribution is at 2.5 to 3.5 μ with a tail out to perhaps 8 μ. The normalized 10.6 μ scattering data suggest substantial increases in particle size to the 4-6 micron range. The scattering at 0.6328 μ suggests the 5-6 μ range. We note that the shape of the 6 μ curve fits the scattering data at 0.6328 μ quite well. Comparing the average value of the x and o points to the values of the 6 μ curves, the 6 μ curve is too high by about 33% at 0.6328 μ and by about 37% at 10.6 μ. The average of the x and o points would correspond to data taken at $\gamma_{0.63}$ of about 0.0135 cm^{-1}. The peak of the true distribution is probably not shifting as much as these results imply, but the fraction of the particles in the tail which strongly influence the forward scattering is probably varying. The relationships between the values calculated by using square distributions and those calculated by using $r^A e^{-Br}$ distributions mentioned in the water fog discussion above also apply to the ice fog data. Thus, the peak of the actual distribution for the ice fogs probably lies between 2.5 and 4 μ.

So far we have considered only the gross characteristics of the ice fogs. Within each run there are small subtleties, most of which are not repeatable and, therefore, not important. Occasionally a small detail is continually repeated so that it demands a sound physical explanation. Consider runs 103 and 111 in Fig. 3-10 which contains curves of $\sigma_{10.6}/\sigma_{0.63}$ versus $\gamma_{0.63}$ on an expanded scale with zero suppressed. Beginning at point 1 on run 103, we see the extinction ratio increase monotonically to point 4, 45 sec later while $\gamma_{0.63}$ has been decreasing. Thus the number of particles is decreasing while the particle size increases. After point 4, there is an abrupt change. $\gamma_{0.63}$ remains essentially constant while the ratio $\sigma_{10.6}/\sigma_{0.63}$ decreases for over 30 seconds. This must mean that $\sigma_{10.6}$ is decreasing with an accompanying decrease in particle size as observed with 10.6 μ radiation. The effect is repeated in dozens of runs. Run 111 shows the same phenomenon later in the morning when the wall temperature was slightly warmer. Runs 113, 121, and 128 were taken in sequence beginning again with a cold wall. All runs exhibit this effect.

The scattering data at 0.6328 μ and 10.6 μ tend to add supporting facts. Figure 3-11 shows two runs which were selected for comparison because the curves' shapes versus time (point number) were considered to be the most representative of all runs. The $\gamma_{0.63}$ scales do not overlap, thus the ordinate and abscissa values must be treated as relative rather than absolute in comparing the two curves. For points 1 through 3, the 10.6 μ scattering is increasing while the visible scattering is decreasing. From then on the 10.6 μ scattering decreases to point 6, while the visible

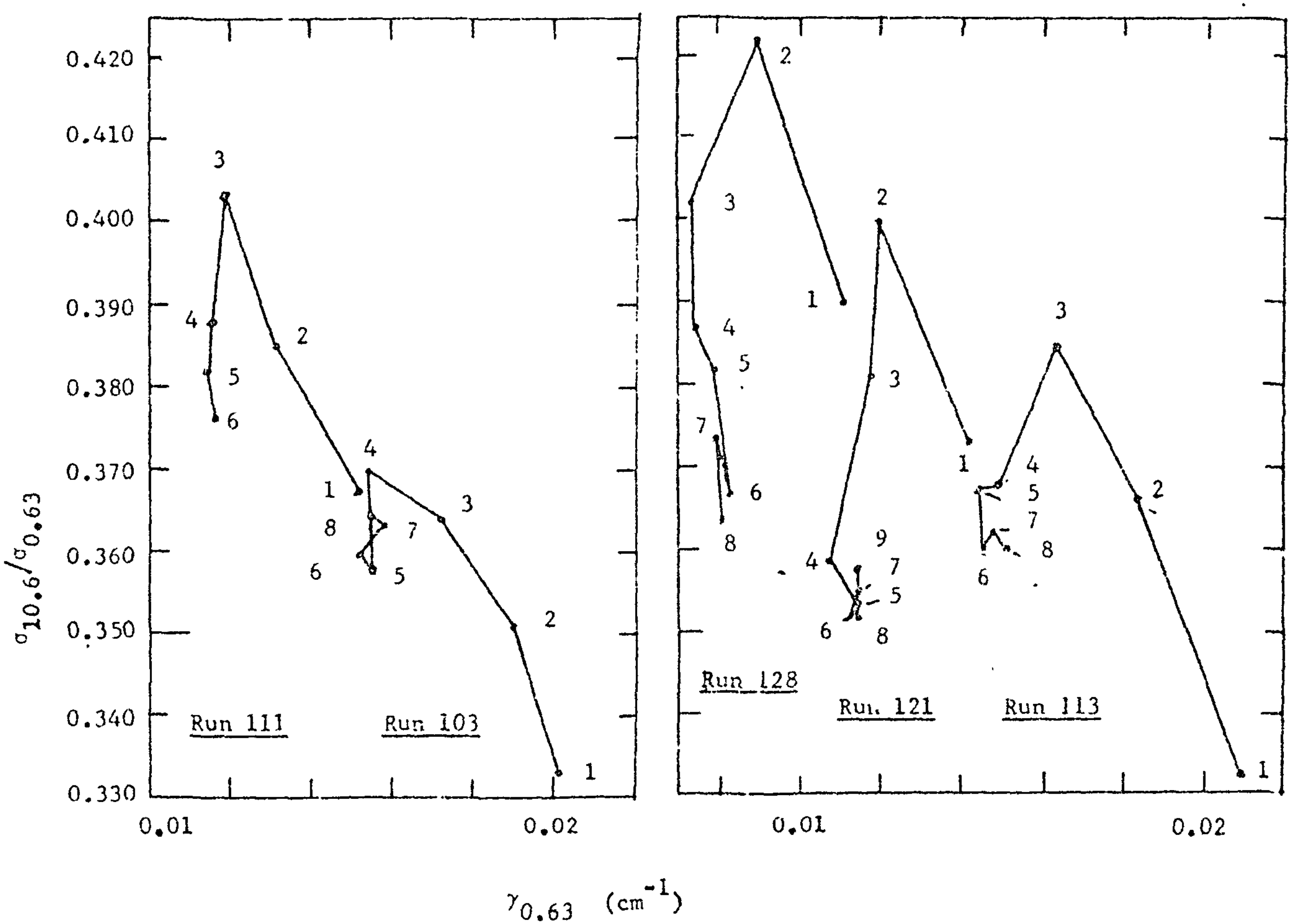

FIG. 3-10. Ratio of the extinction cross-section at 10.6 μ to 0.6328 μ versus $\gamma_{0.63}$ for several independent ice fogs. The time interval between successive numbers is 15 seconds.

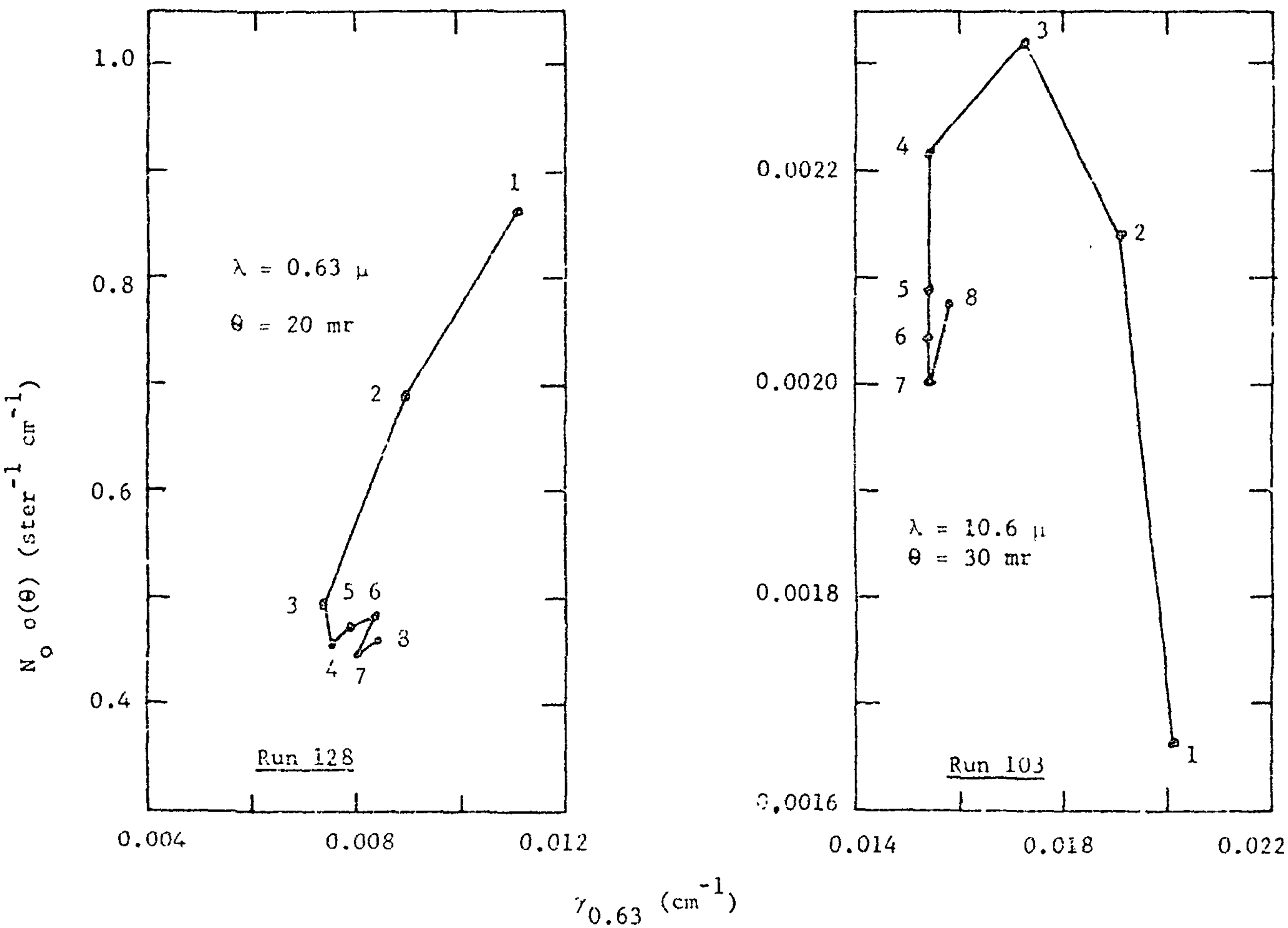

FIG. 3-11. Comparison of scattering at 0.6328 μ and 10.6 μ during the evolution of the ice fog cycle.

scattering is essentially constant. Beyond this point both remain relatively constant. It may be possible to adjust the parameters so that an increase in particle size combined with a simple reduction in N_0 would produce the curves shown between points 1 and 3 in Fig. 3-11. However, after point 3 the explanation becomes more difficult. It appears that the average particle size is decreasing but only as observed at 10.6 μ.

A possible explanation may be found in some recent experiments with ice fog performed by F. K. Odencrantz and P. H. Hildenbrand (Ref. 16). They have reportedly seen via electron microscopy a transient growth of ice whiskers on ice crystals during one of the stages of evolution. The whiskers are unstable and disappear when the crystal stops growing. They reported that the whiskers are 0.5 to 1.0 μ in diameter and can be 5 to 20 μ in length. The spacing between them can be on the order of 5 μ. Most of their work was done at chamber temperatures of -5 to -15°C. If their results are valid and can be extrapolated to our working temperature (i.e., -50°C), the whiskers could explain all of the observations. The whiskers appear as small, widely separated scatterers to the 0.6328 μ radiation and do not significantly influence the forward scattering. However, the distance between the whiskers is less than the 10.6 μ wavelength. Hence the whiskers disturb the wave front and give the particle an effective radius somewhere between the particle radius and the radius at which the whisker separation is about one wavelength. If the assumption is correct, the problem serves to illustrate the utility of the multiple wavelength approach to scattering and propagation. By using two or more wavelengths in performing an experiment, the versatility is greatly increased and deeper insights become possible.

SECTION 4

EXTINCTION BY FOGS BETWEEN 2.3 AND 3.6 MICRONS

Optical Arrangement for Multiple-Wavelength Attenuation Measurements

Radiant energy from a Nernst glower passes through a 450 Hz chopper and is focused onto a 1.5 mm diameter aperture stop. A spherical mirror of 114 cm focal length collimates the energy which has passed through the aperture stop. The resulting beam diameter is 4 cm with approximately 1.3 milliradians divergence. The collimated beam passes through either the ice-cloud chamber or the water-cloud chamber to the receiving optics shown in Figure 4-1.

Spherical mirror M1 focuses the incoming beam onto a circular aperture stop A which limits the field of view of the system to approximately 4 milliradians. The diameter of A is about 50 percent larger than the somewhat astigmatic image formed on it. Stop A thus eliminates most of the scattered and extraneous energy without limiting the primary transmitted beam. Mirror M3 images aperture stop A onto the entrance slit S of a grating spectrometer. Filter F1 eliminates overlapping orders of shorter wavelengths in the grating spectrometer and reflects a portion of the energy onto mirror M4 which in turn images stop A on a PbS detector D. Interference filter F2 restricts the transmitted beam to approximately 0.2 micron band pass centered at 2.45 microns. This filter channel serves as a fixed wavelength reference.

The grating spectrometer employs a 64 mm x 64 mm grating and has 2 exit slits whose wavelength separation is approximately 0.1 micron. The spectral slitwidth of each channel is about 0.005 microns. The exit slits are imaged on PbS detectors which are cooled by liquid nitrogen to enhance their sensitivity to longer wavelength radiation. The spectrometer was used to measure the transmittance of artificial fogs at several wavelengths between 2.3 and 3.6 microns, while the filtered channel simultaneously was used to measure the transmittance at 2.45 microns. Filter F1 was temporarily replaced by a flat glass window to make a few simultaneous measurements at 0.63 and 2.45 microns.

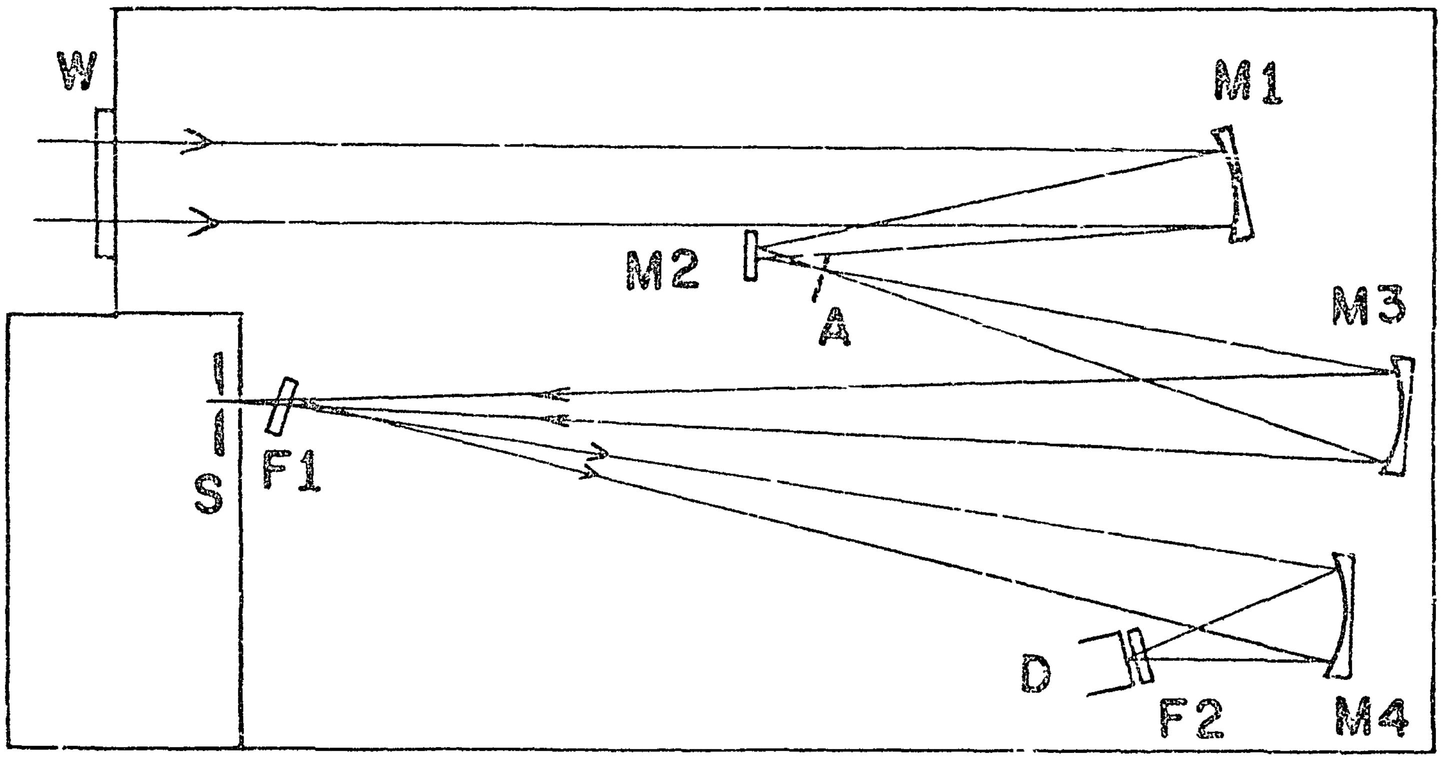

FIG. 4-1. Receiving Optics. The components are enclosed in a plywood box and are as follows: W, CaF_2 window; A, circular aperture; F1, 2 micron long wavelength pass filter and beam splitter; F2, 2.45 micron filter with 0.2 micron band pass; D, PbS detector with 4 mm diameter sensitive element and operated at room temperature; S, entrance slit of grating spectrometer having 2 exit slits and 2 PbS detectors cooled by liquid N_2.

Boxes enclose both the transmitting optics and the receiving optics so that most of the optical path outside of the cloud chamber can be flushed with dry N_2 to reduce absorption by water vapor. This is particularly important near 2.7 μ where H_2O vapor absorption is very strong. Partitions within the receiving optics box further reduce extraneous background radiation to a negligible level.

As the ice clouds form and dissipate, temperature gradients in the chamber produce turbulence which causes fluctuations in the detector output not directly related to changes in cloud density. The turbulence causes greater fluctuations on the spectrometer detector outputs than on detector D in the reference channel. The sensitive element of D is considerably larger than the image formed on it so that the output is not sensitive to small motions of the image. On the other hand, slit S is narrower than the image on it so that image motion due to turbulence undoubtedly produces variations in the detector outputs. The turbulence is greatest when the chamber is first opened and decreases after a cloud has formed. In order to reduce errors in the extinction coefficient caused by turbulence to less than approximately 5 percent, we limited most of the measurements to fogs of at least 50 percent extinction.

Fluctuations in detector signals due to variations in water cloud density were strongly correlated with both time and amplitude for all three detectors. Therefore, errors in the ratios of extinction coefficients resulting from cloud noise are probably less than 2 percent.

Each detector output is amplified by a phase-sensitive amplifier and displayed on a strip chart recorder. The recorder chart drives are synchronized and run at the same speed. The speed can be varied continuously during a measurement, making it possible to spread out portions of the chart where the deflection is changing rapidly without making the total chart length excessive. Amplifier time constants of 0.1 sec were employed in order to preserve fast changes in the signals. Maximum recorder pen speeds are approximately 0.5 seconds for full-scale deflection. Representative recorder tracings are shown with the discussion of the results.

Experimental Results for Water Fogs

The transmittances of several samples of water fog have been measured at selected wavelengths between 2.3 and 3.6 microns with the equipment described above. Figure 4-2 shows the recorder deflection as a function of time for a typical water fog. The spectrometer monitored the transmitted beam at 2.82 μ and 2.92 μ in this example. The water fog cycle is produced by first allowing the chamber to come to equilibrium with a saturated atmosphere at a temperature of about 20°C. Then, liquid nitrogen is flowed through cooling coils at the top of the chamber to

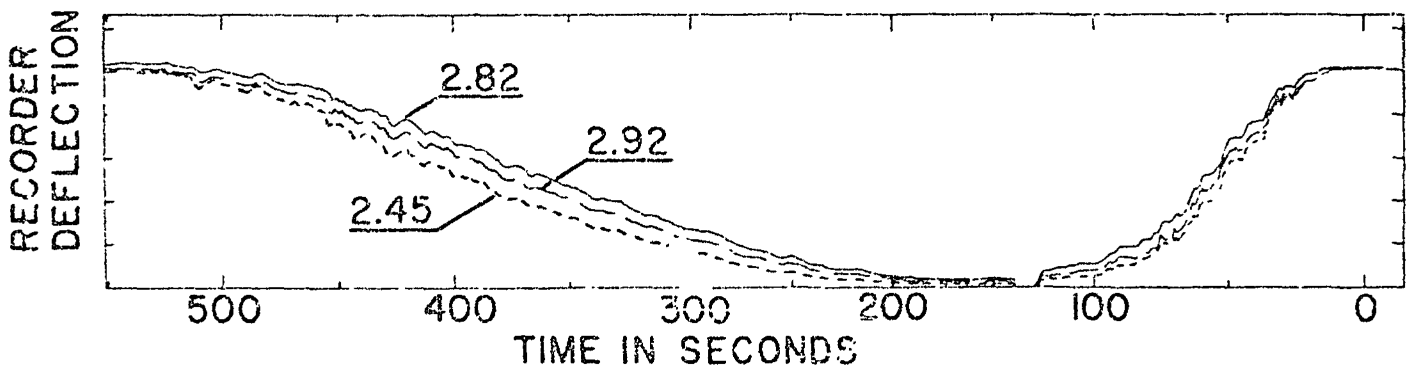

FIG. 4-2. Recorder deflection versus time for a typical water fog cycle. The curves are identified by wavelength in microns.

chill the atmosphere in the chamber and create a super-saturated condition which leads to fog. The time scale in Fig. 4-2 arbitrarily starts at the time the liquid nitrogen commenced flowing through the cooling coils. The duration of the nitrogen flow for this run was 90 seconds. As shown in the figure, however, the density of the fog continues to increase until about 170 seconds after the start of the nitrogen flow. This is partially due to the thermal mass of the cooling coils which continue to cool the chamber after the nitrogen has stopped flowing. The continued growth of fog particles may also contribute to the increase in density.

Note that at the end of the run the transmission of the 2.82 μ channel is higher than at the beginning. This is caused by a decrease in the amount of water vapor within the chamber during the run and the corresponding decrease in water vapor absorption. Wavelengths are generally chosen where the H_2O vapor absorption is minimal, but some absorption cannot be avoided in the strong part of the H_2O vapor absorption band. Further, the wavelength separation between the two spectrometer slits is fixed at 0.1 μ; therefore, only one of the wavelengths can be set at an absorption minimum. In cases of excessive absorption, we only consider data for which the fog transmittance is less than approximately 10 percent to minimize errors due to vapor absorption.

The beam was blocked during the short period of zero transmission encountered at about 125 seconds; this was done in the area of the minimum transmission of every run to reduce errors in the analysis produced by shifts in the zero level. The small scale structure which occurs simultaneously in the three curves is caused primarily by variations in the fog density and by turbulence in the air. When the structure becomes too fine, the spectrometer channels show direct correlation within the structure, but the structure is lost on the filter channel. As mentioned in the equipment description, this is probably caused by the spectrometer entrance slit being narrower than the image formed on it, while the only limiting stop in the filter channel is the system's entrance aperture. Figure 4-2 shows the transmittance to consistently decrease from 2.82 μ to 2.92 μ to 2.45 μ. This indicates that the extinction coefficient increases progressively from 2.82 μ to 2.92 μ to 2.45 μ.

Only the portion of the cycle after the fog had reached minimum transmittance was considered in the data reduction. During this time the particle-size distribution is probably changing more slowly and more nearly represents natural fogs, although the number density is probably higher than in natural fogs. The 2.45 μ curve was used to select times when data points were taken. Intervals corresponding to approximately 10 seconds were chosen when the average transmittances at 2.45 μ were 5, 10, and 50 percent. The average transmittances during these same ti periods at the other two wavelengths were then determined from the cu_ es. Ratios of the extinction cross-sections $\sigma_\lambda/\sigma_{2.45}$ were then calculated. Essentially no forward scattered radiation was detected, so this ratio is equal to the corresponding ratio ($\ln T_\lambda / \ln T_{2.45}$). Throughout this section σ denotes σ_{ext}, and σ-ratio at λ means ($\sigma_\lambda/\sigma_{2.45}$). As discussed previously, the σ-ratio at a particular wavelength is independent of N_o, the particle density, provided the particle-size distribution remains constant.

The lower panel of Figure 4-3 presents a plot of the σ-ratios for all of the data obtained with the water fog chamber operating in its normal cycle. The solid, top curve is drawn through the circles and the squares. The lower, dashed curve is drawn through the x's. In plotting the curve, the 5 and 10 percent points were grouped together since there is considerable overlap between them. The 50 percent points were considered separately since they consistently fall below the other two values. A simple average of the σ-ratio was taken for the points at each wavelength to determine the location of the curve. A variation in the particle-size distribution during the dissipation of the fog is implied by the separation of the curves.

The upper two-panels of Figure 4-3 contain spectral plots of the imaginary (n_i) and real (n_r) parts of the complex index of refraction for water. The curves are based on values tabulated by Irvine and Pollack (Ref. 9), and these values are used for calculating theoretical σ values. These index values are probably subject to sizeable errors because of the difficulty in measuring these quantities in this region where both n_i and n_r change rapidly and n_i attains large values. Nevertheless, these curves provide the basis for an explanation of the σ-ratio curves. The minimum in $\sigma_\lambda/\sigma_{2.45}$ at about 2.75 μ is undoubtedly related to the minimum in n_r at the same wavelength. At 2.75 μ, n_i is sufficiently small that the influence of n_r dominates for particle sizes typical of our normal fogs. The 2.45 μ reference wavelength was chosen to be near the regions of rapid change in n_i and n_r for ice and water. Consequently, for a given particle size, differences in the size parameters at the reference wavelength and at the other wavelengths of interest are small and changes in σ_λ are due primarily to changes in n_i and n_r.

Further discussions of the σ-ratio curves are referred to the calculated curves in Figures 4-4 and 4-5 which are based on values of n_i and n_r from Figure 4-3. A Mie theory computer program was employed to calculate σ for the particle-size distributions indicated in these figures. Particle-size distributions, rather than individual particle sizes, were used for the larger particles in order to smooth out some of the influence of resonances. The $4 \leq r \leq 8$ μ curve in Figure 4-4 exhibits a Mie theory resonance which completely obliterates the "window" which occurs near 2.7 μ wavelength for smaller particles. The curve representing the 8-12 μ size distribution illustrates the smoothing of individual particle resonances by integration over a large size distribution. These points also infer the well-known result of Mie theory that σ becomes nearly independent of n_r and n_i

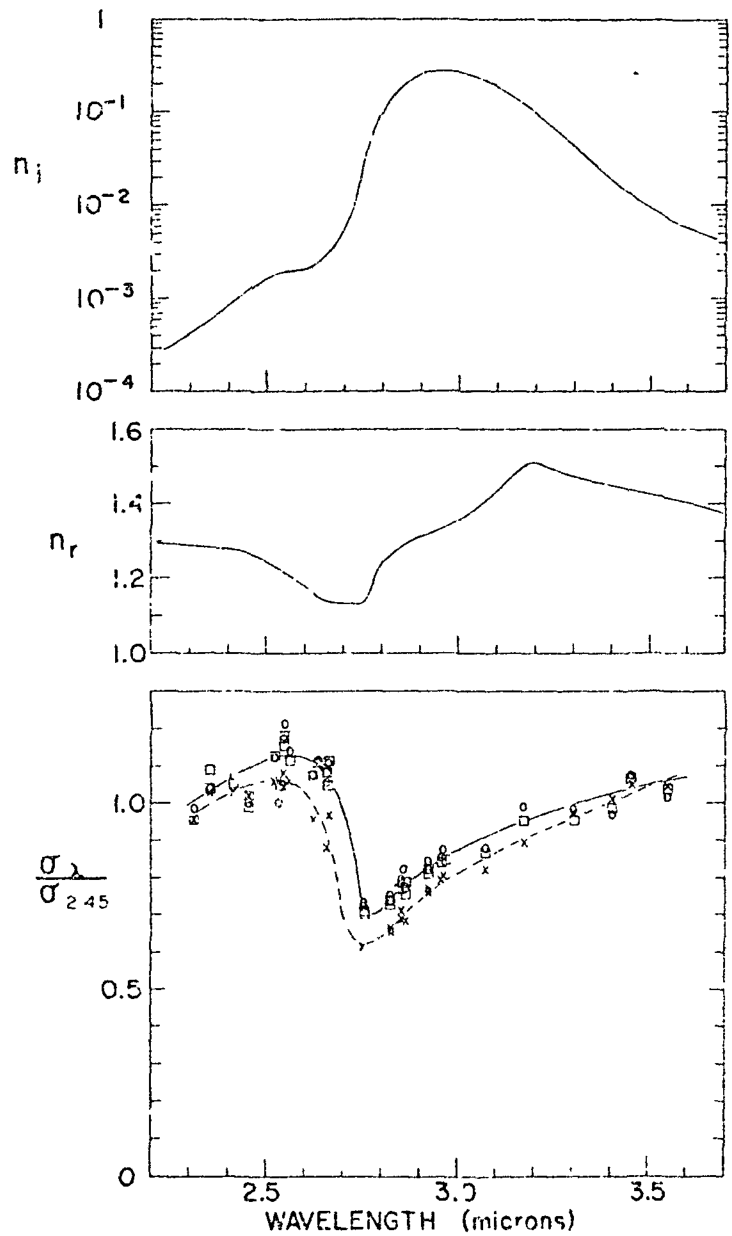

FIG. 4-3. Spectral curves of n_i and n_r for water and observed σ-ratios for water fogs. The data were taken at values of $T_{2.45}$ as follows: ○, 0.05; □, 0.1; x, 0.5.

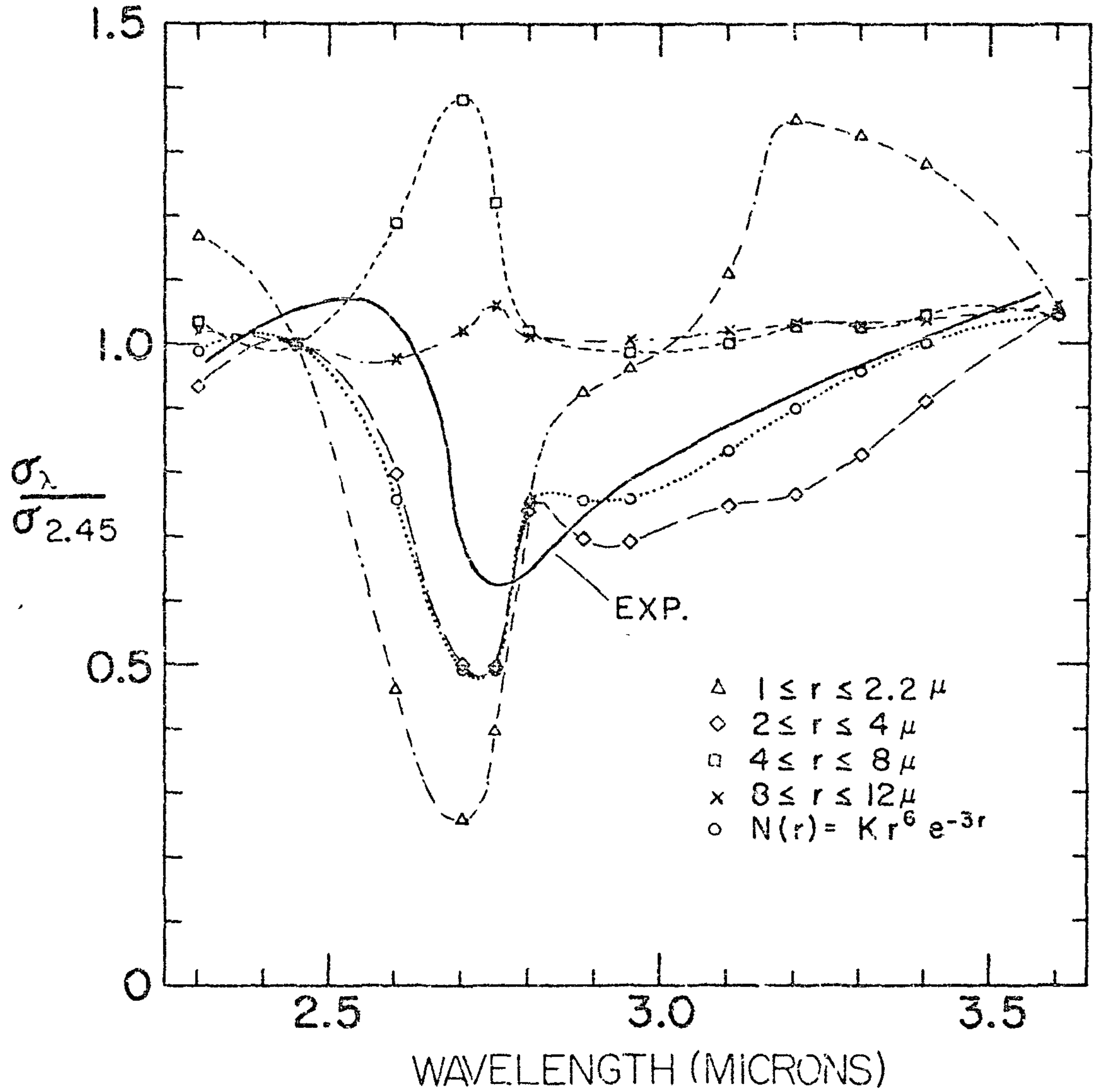

FIG. 4-4. Spectral curves of calculated σ-ratios for various particle-size distributions for water. Except for the Kr^6e^{-3r} distribution, N(r) is constant for particle radii within the interval shown and zero elsewhere. The solid curve is the lower experimental curve from Fig. 4-3.

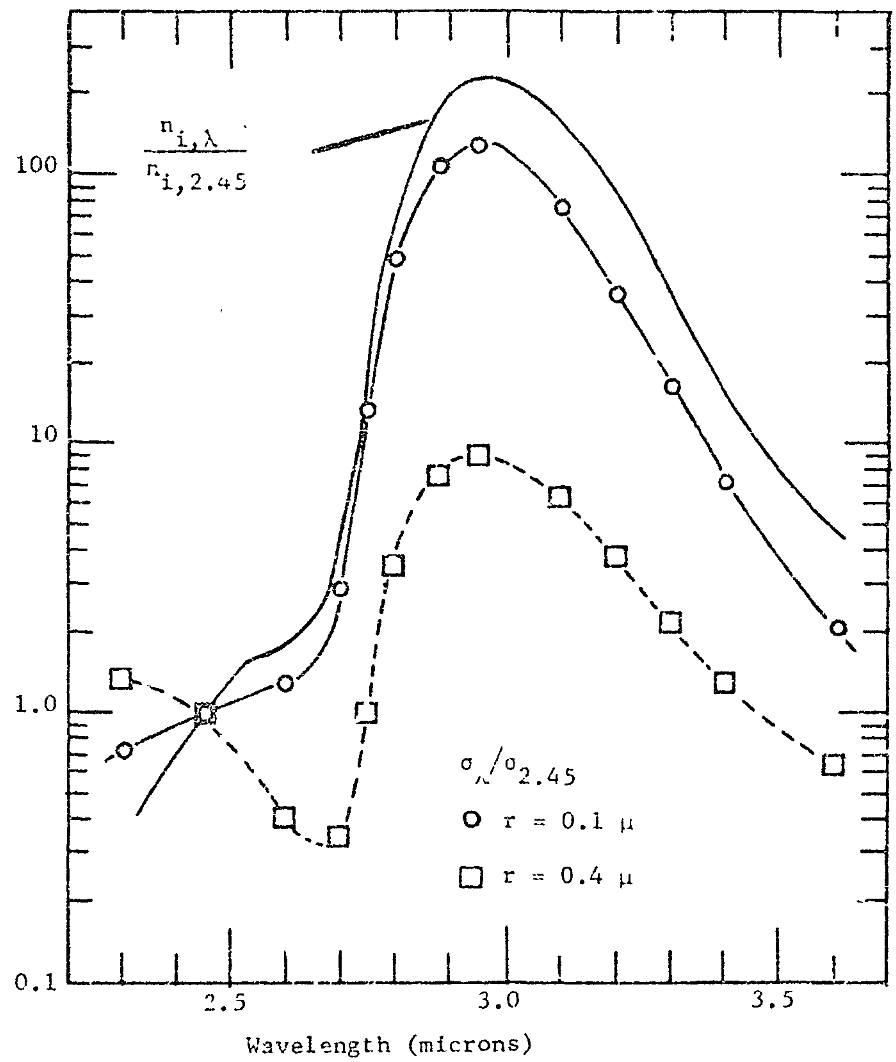

FIG. 4-5. Spectral curves for water of the imaginary index ratio and the c-ratios for r = 0.1 and 0.4 μ radius particles.

for $r \gg \lambda$, particularly if n_i is not too small. Thus, the σ-ratios approach unity for this condition. Because of the smoothing of the resonances, the σ-ratios approach unity for a wide distribution containing small particles even though these particles individually exhibit strong resonances.

The curves in Figure 4-4 for intermediate size distributions demonstrate the strong dependence of the shapes of the σ-ratio curves on particle size in regions where n_i and n_r change rapidly. Minor changes in the particle-size distribution during the dissipation of the fog can account for the separation between the two experimental curves in Figure 4-3. The calculated curves suggest further that a major portion of the particles in our fogs lie between 2 and 4 μ radius. This result is consistent with those discussed in Section 3. Thus, the σ-ratio curve for the distribution $N(r) = Kr^6 \exp(-3r)$ used in Section 3 was calculated and is shown in Figure 4-4. The curve for this distribution provides a better fit to the experimental data than the other calculated distributions, although the difference between this curve and the one corresponding to the 2 to 4 μ square distribution is small. It appears that it would be difficult to derive a realistic particle-size distribution which would fit the experimental curve on both the short wavelength and long wavelength sides of the minimum. Because of the uncertainty in the tabulated values of n_r and n_i, it is likely that these quantities need to be adjusted. The effects of Mie theory resonances are considered in more detail in the following section on ice fogs.

Figure 4-5 further demonstrates the strong dependence of σ on n_i when $r \ll \lambda$ and n_i is large. Two of the curves are spectral plots of the σ-ratio for $r = 0.1$ and $0.4\ \mu$. The other curve represents $n_i(\lambda)/n_i(2.45)$. We note that between approximately 2.8 and 3.6 μ wavelength where n_i is large, the n_i ratio curve and the $r = 0.1\ \mu$ σ-ratio curve are nearly the same in shape. This implies that at a given wavelength σ is nearly proportional to n_i for these very small particles. For even smaller particles the same relationship should hold. The peak of the σ-ratio curve for the 0.1 μ particles is 127, which is much larger than the corresponding value of 9.1 for the 0.4 μ particles. Thus, 0.4 μ radius particles are not sufficiently small nor is n_i sufficiently large for σ to be directly proportional to n_i, even at $\lambda = 2.95\ \mu$.

In order to show experimentally the effects of the size distribution and to explore the stability of the size distributions produced by the fog chambers, we have studied several fog samples produced by extreme variations from the normal fog cycles. A striking example of the influence of small particles is shown in Figure 4-6. Both the recorder deflection and the σ-ratio are plotted as a function of time throughout the evolution of the fog. The fog was produced in the water fog chamber by directing a stream of liquid nitrogen lengthwise through the top of the chamber. The recorder deflection at 2.95 μ, which corresponds to the peak of the imaginary index of refraction, decreased most rapidly and remained consistently less than at the other two wavelengths.

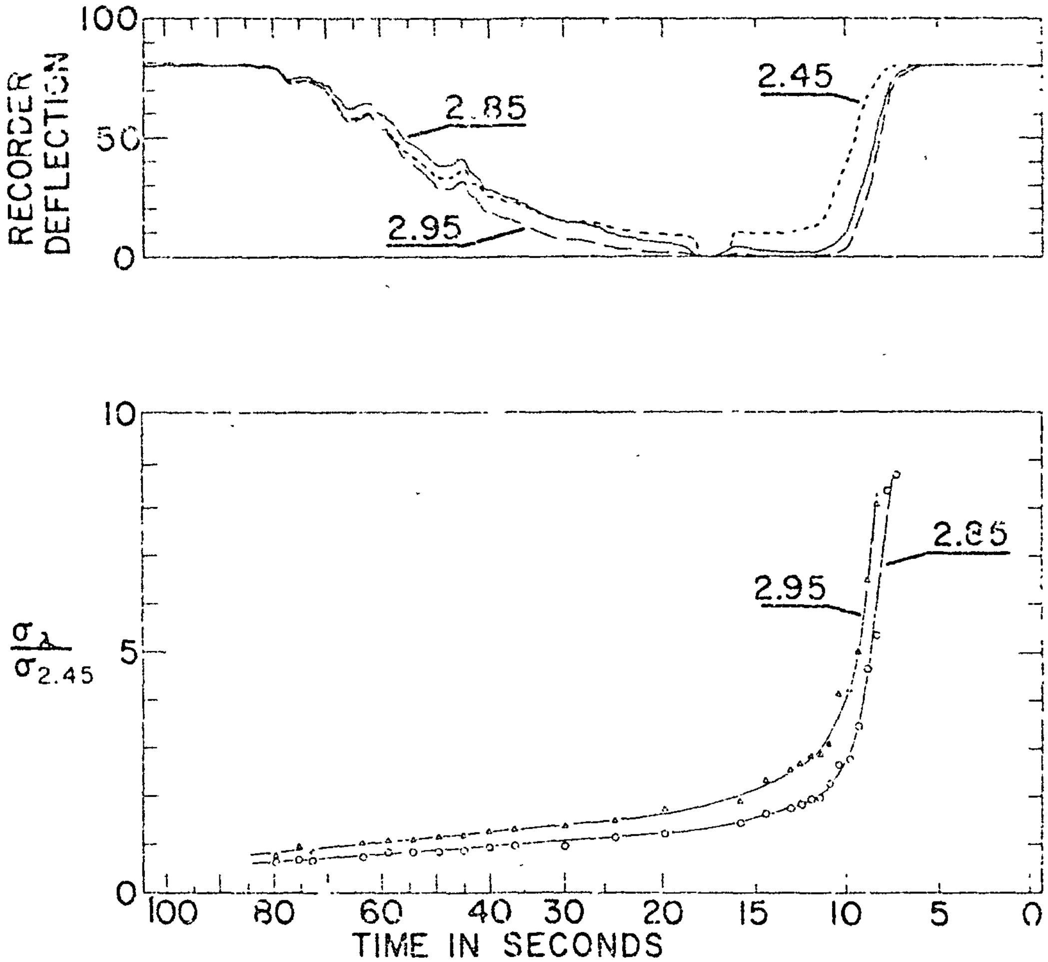

FIG. 4-6. Recorder deflection and σ-ratios versus time for a water fog generated by introducing liquid nitrogen directly into the fog chamber. The curves are identified by wavelength in microns.

As seen in the σ-ratio plot, the 2.95 μ extinction cross-section was initially much larger than at 2.85 μ or 2.45 μ and was always larger than at 2.85 μ. The σ-ratio curves also demonstrate that initially the particle sizes were quite small. The first point shown on the run corresponds to a particle radius between 0.1 and 0.2 μ. Further, as the run progressed in time the particles grew rapidly and became reasonably uniform in size, as is indicated by the very gradual slope of the σ-ratio curves for times greater than 20 seconds. The time scale arbitrarily starts at the time the liquid nitrogen was turned on; for this particular cycle the duration of liquid nitrogen flow was 12 seconds. The chamber air temperature varied between 8 and 15°C as read with a mercury thermometer. The σ-ratio curves maintain a gradual slope, indicating an increase in particle sizes up to 80 seconds, whereupon the changes in deflections were too small to read. This implies that the particles continue to grow even toward the end of the cycle, and that the increase in transmission during the latter part of the cycle is due to a decrease in particle density rather than to a simultaneous decrease in particle size and density. Although this appears valid for this extreme case of fog generation, a normal fog cycle consumes much more time, and it is likely that both the particle size and density decrease toward the end of the run.

Two other techniques were employed in an attempt to generate particle-size distributions different from the norm. One technique consisted of heating the water trays in the water fog chamber to about 70°C, whereas the normal temperature was about 20°C. In addition, the chamber air was heated to between 45°C and 70°C before flowing the liquid nitrogen through the cooling coils. We designate this as our "hot technique". The other technique consisted of forming super-cooled water fog within the ice cloud chamber at about -23°C. We call this the "cold technique".

Figure 4-7 shows experimental values of the σ-ratio for the various types of water fogs. The values shown on the figure are average values for a run at a given wavelength; the average is weighted linearly in time from about four seconds after the liquid nitrogen is turned off, until the difference in recorder deflection between channels is too small to read. The average value is the center of the circle for the hot water case and the center of the diamond for the direct liquid nitrogen case; the bracket about each point designates the range of fluctuation of the σ-ratio during the run. Not shown in the figure are values previous to four seconds after termination of the liquid nitrogen flow. These early values always correspond to smaller particles than those present during the time over which the average was taken. The solid curve in the figure is a re-plot of the σ-ratio for the lower curve in Figure 4-3 for a normal water cycle.

We note that only the fog produced by flowing liquid nitrogen directly into the chamber deviates significantly from the normal fog curve. Since this technique was the most radical one, and also the one which produced the smallest particles, it is to be expected that the deviation from

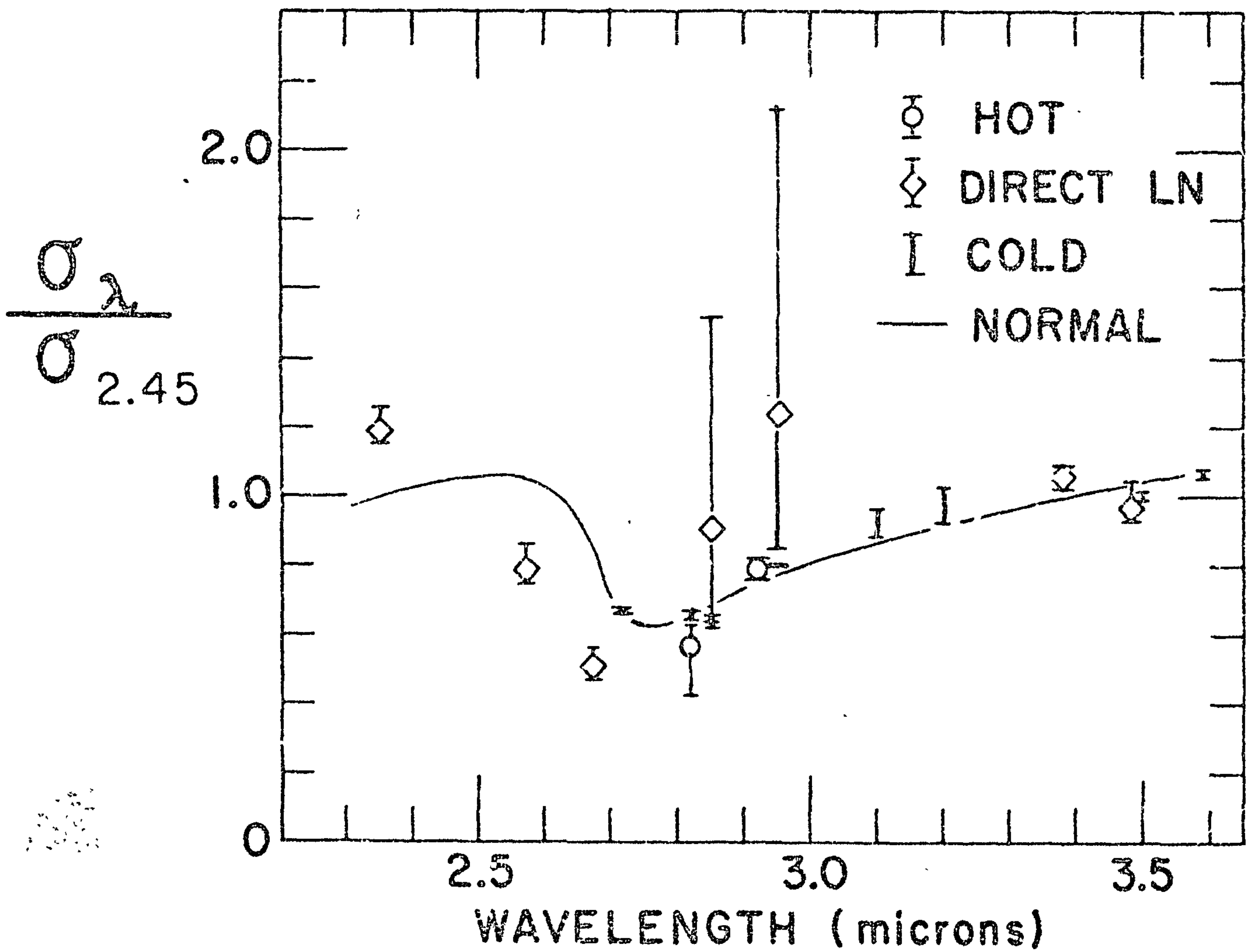

FIG. 4-7. Observed c-ratios versus wavelength for water fogs generated under various conditions. The solid curve is the lower experimental curve from Fig. 4-3.

the normal curve would be greatest. However, it is of interest that points corresponding to the fogs produced by the other techniques lie quite close to those for the normal fog. In fact, they are reasonably well within the spread of normal fog data. Therefore, we conclude that the water fog size distribution produced within a normal cycle is moderately stable, and that the σ-ratio curves resulting from these fogs represent a given size distribution with only small errors due to changes in particle sizes from cycle to cycle.

Experimental Results for Ice Fogs

The transmittance of ice fogs at selected wavelengths between 2.3 and 3.5 μ was measured in the same manner as described above for water fogs. The ice fogs were generated by the same technique used in the near-forward scattering experiment. The ice fog cycle is initiated by capping the chamber ends and allowing the system to equilibrate at a temperature between -47 and -51°C. Then, the end apertures of the chamber are simultaneously opened and room air at approximately 50 percent relative humidity flows into and mixes with the cold chamber air. Ice crystals form spontaneously within the chamber and initially grow in size. Later in the cycle, they stabilize in size and number. The equilibrium size is between the larger particles found during the growth process and the small particles found at the beginning of the cycle. The air temperature within the chamber increases about 2°C during the cycle. At the end of each cycle, the end apertures are closed, and the chamber air cools to near equilibrium before the next cycle is started.

Figure 4-8 shows a typical example of recorder deflection as a function of time for an ice fog. As for water fogs, the filter channel remained at 2.45 μ wavelength. The time scale commences with the beginning of a zero-transmittance check; the sudden increase in transmittance corresponds to the opening of the end apertures. The elapsed time during the cycle is shorter here than during the near-forward scattering experiment. This is probably due to possible differences in room humidity and to the tighter fitting end caps used during these later cycles. Upon opening the ends, the particles grow rapidly for about 25 seconds, after which the larger particles fall out and the average particle size decreases to an equilibrium value at about 80 seconds. The transmittance values used in calculating σ-ratios were read from the curves at the point of minimum deflection on the 2.45 μ curve and at several locations in increasing time from this point. From the relative positions of the curves in the figure, it is apparent that $\sigma_{2.83}/\sigma_{2.45}$ is less than $\sigma_{2.93}/\sigma_{2.45}$ and that both are less than unity.

The lower panel of Figure 4-9 shows the observed σ-ratio for ice fogs. The curve is drawn through an average of points obtained with $T_{2.45}$ ranging from 4 percent to 60 percent. The ratios did not show any consistent progression in value as $T_{2.45}$ increased during the dissipation of the fog. Therefore, the spread in the data points represent noise within the data.

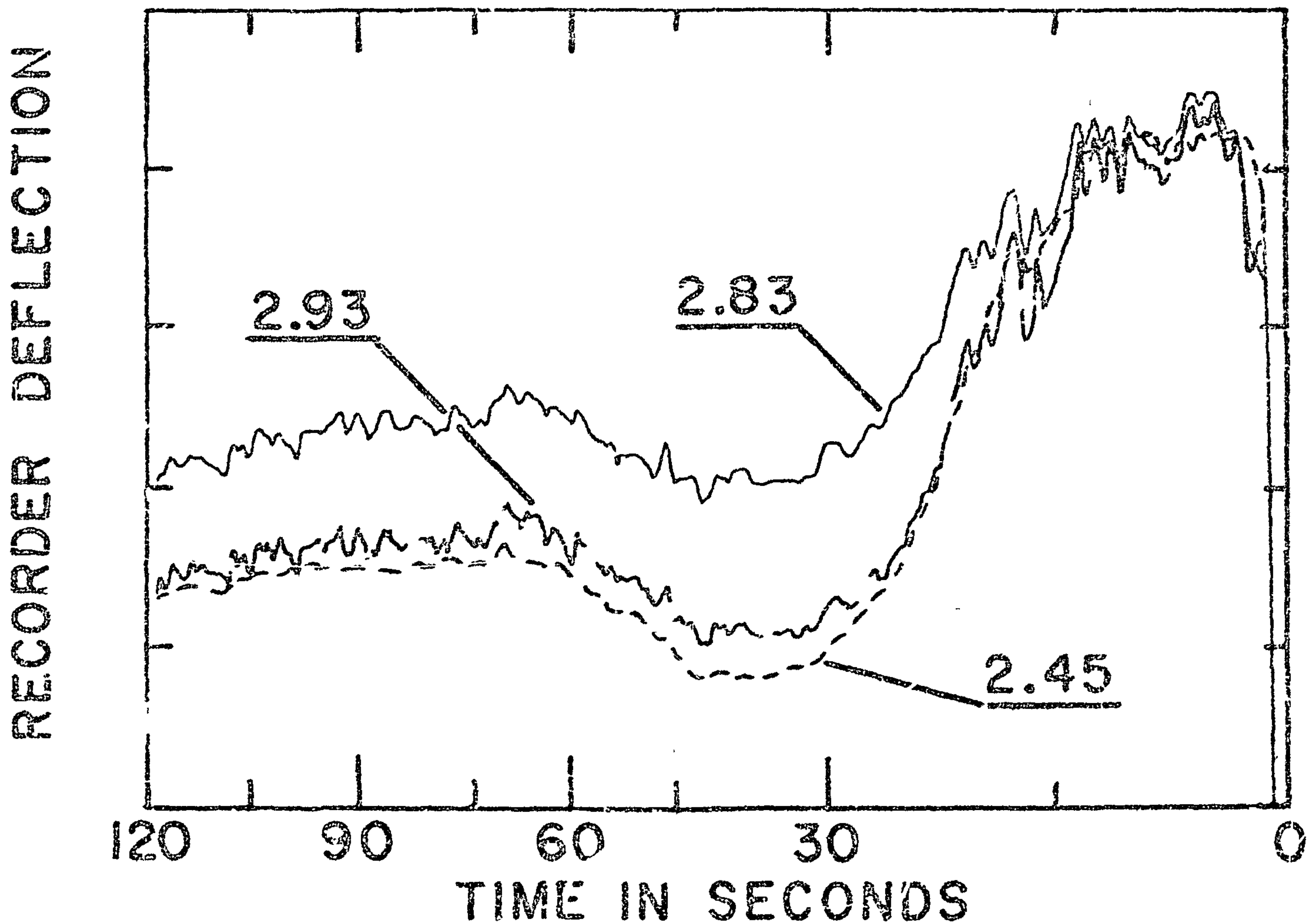

FIG. 4-8. Recorder deflection versus time for a typical ice fog cycle. The curves are identified by wavelength in microns.

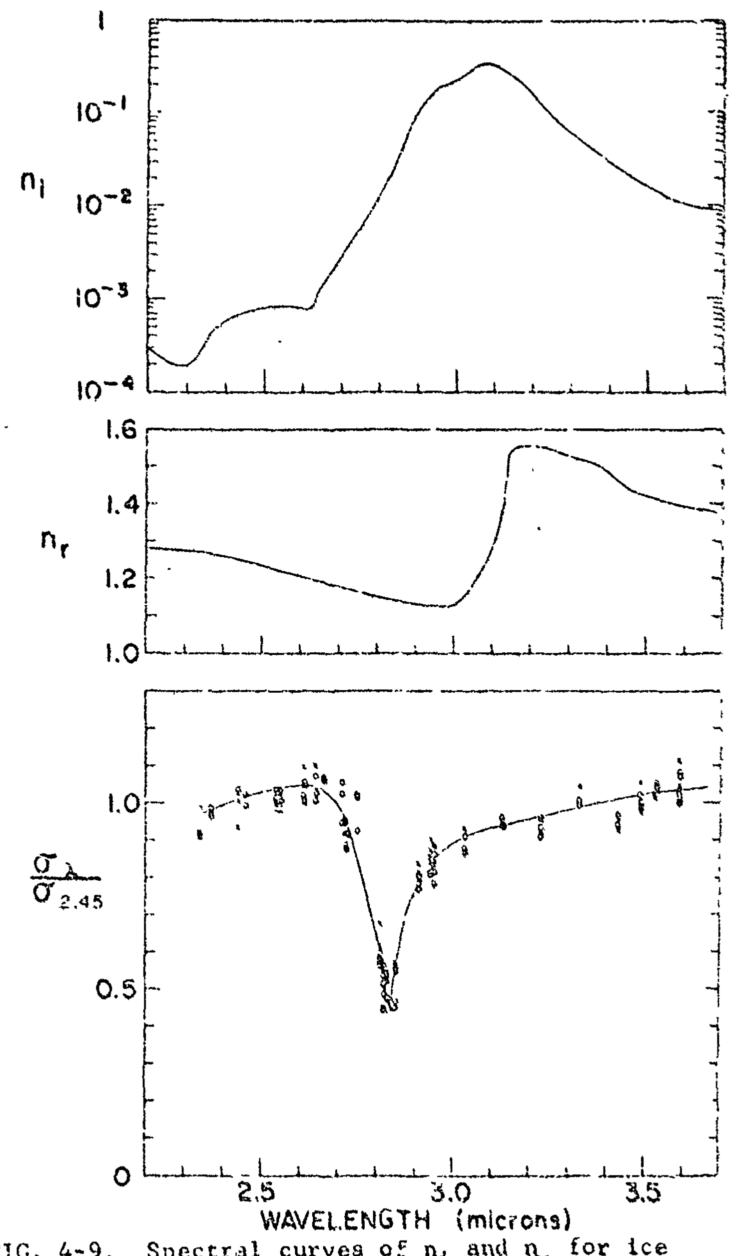

FIG. 4-9. Spectral curves of n_i and n_r for ice and observed σ-ratios for ice fogs. The observed data were taken at $T_{2.45}$ between 0.04 and 0.3 for the circles and $T_{2.45}$ between 0.31 and 0.6 for the x's.

To avoid possible errors caused by a gradual change in the environmental factors controlling the particle-size distribution, the selection of wavelength was made at random for sequential runs until data were acquired at all wavelengths of interest. The process was then repeated several times at the more interesting wavelengths. As in the water fogs discussed above, data were taken at three wavelengths simultaneously during each run.

In order to explore the possible effects of a different size distribution or particle shape, we made a few measurements between 2.72 and 3.23 μ with ice fogs produced by a different scheme. The ice chamber was at about -20°C and contained a super-cooled water fog. Silver iodide was added as a seeding agent to cause the formation of ice particles at the expense of the water particles and H_2O vapor. The values of the σ-ratio between 2.72 and 3.23 μ for the seeded ice fogs were always lower than for the normal ice fogs. The general shape of the σ-ratio curve for the seeded ice fog was similar to and had a value of about 80 percent of the σ-ratio curve for normal ice fogs.

The optical arrangement was modified to make a few measurements at 0.63 μ. Values of $(\sigma_{0.63}/\sigma_{2.45})$ varied between approximately 0.83 and 0.98, with no apparent difference between the seeded fogs and the normal ice fogs.

Tabulated data by Irvine and Pollack (Ref. 9) form the basis for the curves of n_i and n_r for ice in Figure 4-9 and were used for the calculations discussed below. Figure 4-10 shows calculated σ-ratio curves for several size distributions of ice particles. A Mie theory computer program was employed to calculate the σ-values used in the ratios. The curves are for distributions with N(r) constant over the intervals indicated, and zero at all other values of r. The gross difference between the shape of the 2-4 μ curve and the 4-8 μ curve is due to resonances.

The influence of particle size or the σ-ratio curve is illustrated further in Figure 4-11. For clarity, only a representative selection of the σ-ratio curves for narrow particle-size distributions are shown. Let us now identify a given σ-ratio curve for a narrow particle-size distribution by the mean particle radius within the distribution. The effects of Mie theory resonances are clearly shown in the 2.7 to 2.8 μ wavelength region. The σ-ratio increases very rapidly to a maximum of about 1.8 as the mean particle size increases from 1.2 to 5.5 μ. As the particle size continues to increase, the σ-ratio quickly decreases to about 1.1 for a mean particle size of 7.5 μ. No larger particle-size distributions were calculated. The strong influence of large n_i is observed near 3.2 μ wavelength for small particles.

Figure 4-12 shows plots of $Q_{ext} = \sigma_{ext}/\pi r^2$ versus particle radius for three different wavelengths. At any given radius, $\sigma_\lambda/\sigma_{2.45}$ is equal

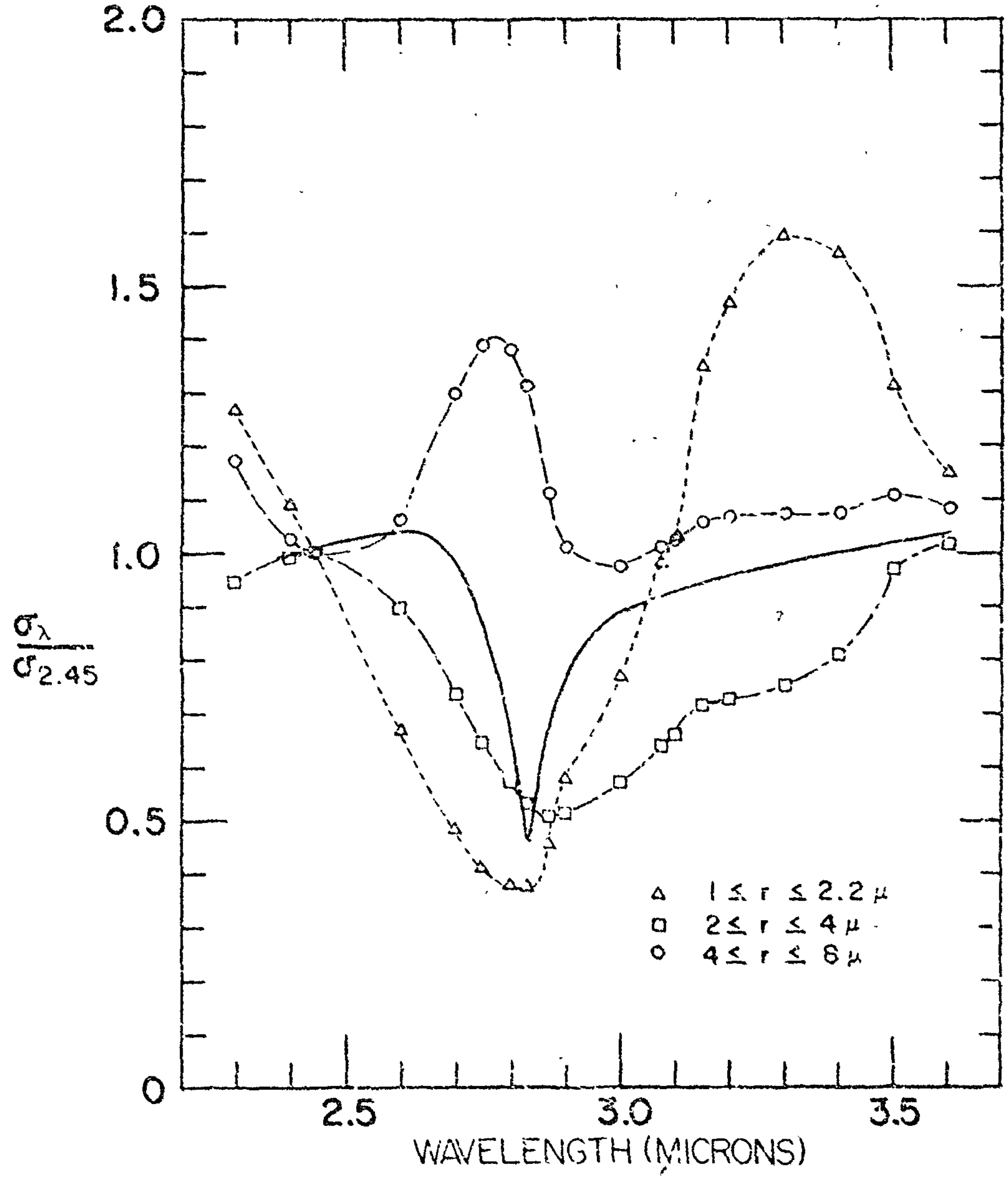

FIG. 4-10. Spectral curves of calculated σ-ratios for various particle-size distributions for ice. N(r) is constant for particle radii within the intervals shown and zero elsewhere. The solid curve is the experimental curve from Fig. 4-9.

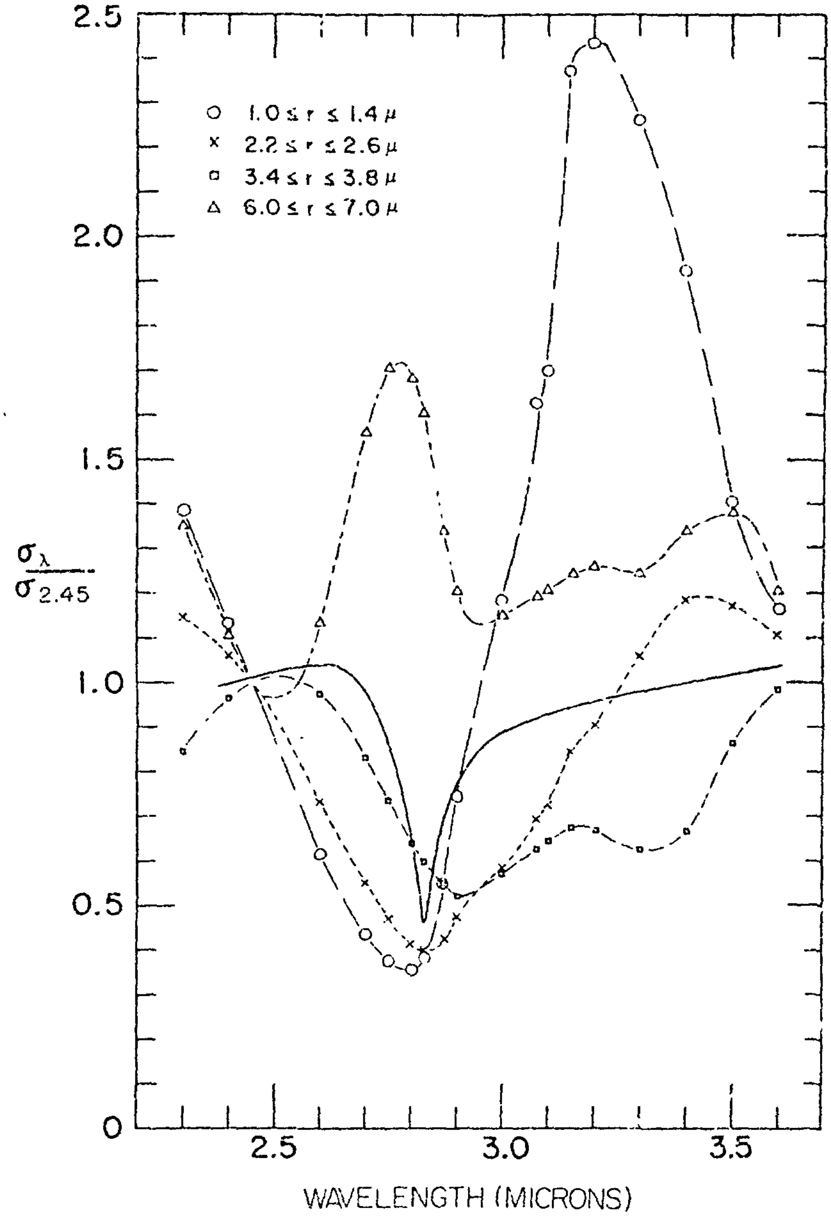

FIG. 4-11. Spectral curves of calculated σ-ratios for various particle-size distributions for ice. N(r) is constant for particle radii within the intervals shown and zero elsewhere. The solid curve is the experimental curve from Fig. 4-9.

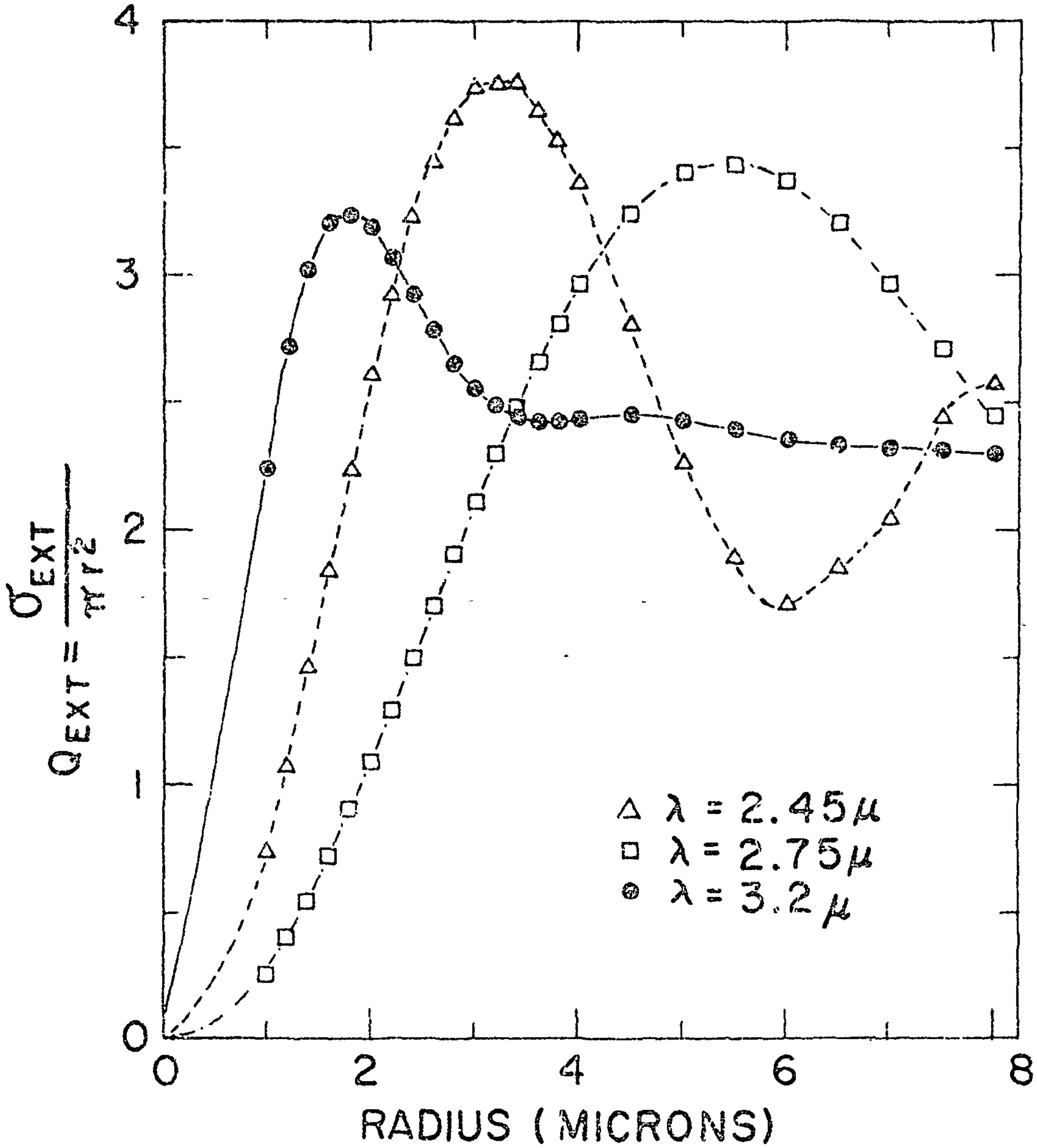

FIG. 4-12. Calculated curves of extinction efficiency versus ice particle radius for three wavelengths.

to $Q_\lambda/Q_{2.45}$, thus the progression of σ-ratio with changing particle radius can be visualized from Figure 4-12 at the 2.75 and 3.2 μ wavelengths. Since n_i is large at the 3.2 μ wavelength, the $Q_{3.2}$ curve is highly damped and shows little oscillation after its initial maximum. Conversely, n_i is small at 2.45 μ wavelength, and the $Q_{2.45}$ curve shows little damping. Scrutiny of the curves in Figure 4-12 also shows that the effects of Mie theory resonances on the σ-ratio will decrease as the particle-size distribution widens.

The curves of n_i and n_r for ice in Figure 4-9 are similar to the corresponding curves for water in Figure 4-3. Therefore, similar σ-ratio curves would be expected for particles of approximately the same size. Indeed, comparison of Figures 4-3 and 4-10 shows that the calculated σ-ratio curves representing the same particle sizes are similar for water and ice. Note, however, that the minimum in the experimental σ-ratio curve for ice fogs is much narrower and sharper than the corresponding minimum for the water fogs. Further, the minimum in the water-fog curve coincides in wavelength with the minimum in n_r and a sub-minimum in n_i, but this is not the case for the ice fogs. The minimum in the σ-ratio curve for the ice fogs occurs at about 2.83 μ, while the minimum in n_r is near 3 μ. The rapid change in n_i between 2.8 and 3 μ may account for part of the displacement between the minima. The influence of the peak in n_r near 3.2 μ on the σ-ratio curve is complicated by the large value of n_i. Irvine and Pollack (Ref. 9) state that the indices between 2.8 and 3.6 μ are very difficult to measure, especially for ice, and that sizeable errors may exist in their tables of the indices of refraction between 2.8 and 3 μ.

Blau, et al. (Refs. 3,4) have observed a "window" centered near 2.8 μ in natural ice clouds. This window undoubtedly corresponds to the minimum in the σ-ratio curve near 2.83 μ. Differences in spectral resolution of the two instruments and in the amount of water vapor absorption could account for the shift in wavelength of maximum transmittance. As a result of their cloud data and of measurements on the scattering properties of mirrors and windows coated with ice frost, Blau, et al., have concluded that the values of n_i and n_r tabulated by Irvine and Pollack are in error near 2.8 μ.

The extinction and near-forward scattering data for our ice fogs discussed in Section 3 indicate that the peak of the particle-size distribution lies between 2.5 μ and 4 μ radius. Examination of the calculated σ-ratio curves in Figure 4-11 and the Q_{ext} curves in Figure 4-12 indicate that the distribution peak must fall between about 1.6 and 3.6 μ radius to even grossly fit the experimental σ-ratio curve. Several σ-ratio curves for distributions of the form $N(r) = r^A \exp(-Br)$ with peaks from 2 to 3 μ were calculated. These curves were all similar in shape and value to the $2 \leq r \leq 4$ μ curve shown in Figure 4-10; none of them provided a reasonable fit to the experimental ice data. The calculated window is wider for all distributions than is the observed window.

Since our results on ice fogs are self-consistent and in general agreement with those of Blau et al., we conclude that the indices of refraction tabulated by Irvine and Pollack (Ref. 9) contain significant errors near 2.8 μ. As improved values of these quantities become available, new σ-ratio curves should be calculated and compared with the experimental results.

SECTION 5

CONCLUSIONS

Techniques have been developed for generating artificial water fogs and ice fogs in chambers which permit measurements of the extinction and scattering properties. The particle-size distribution of the water fogs has its maximum near 2 μ radius and is similar to that of natural fogs. During their growth, the particles in ice clouds display some unusual scattering and attenuating behavior which is probably associated with their irregular shapes. The maximum of the particle-size distribution for the ice clouds after they have come to equilibrium is about 3 μ radius.

Simultaneous measurements of the extinction and near-forward scattering at 0.6328 μ and 10.6 μ indicate that Mie theory is applicable for water fogs. There is also good agreement between calculated values based on Mie theory and experimental results for ice clouds after the particles have passed through their initial phase of rapid growth. Because of the irregular shapes of ice particles, Mie theory is probably not applicable to scattering at angles greater than a few degrees. It also may not be appropriate for particles which are much larger than those studied. The power at 10.6 μ scattered into a unit solid angle is essentially independent of scattering angle at angles less than about 50 milliradians for both the ice fogs and the water fogs. At 0.6328 μ, the scattered power decreases with increasing angle at a rate which is dependent on the particle sizes.

A narrow window occurs near 2.75 μ in water fogs and near 2.83 μ in ice fogs. The extinction coefficient may be less than half as great in the center of one of these windows as at wavelengths displaced by only 0.1 to 0.2 μ. The shape of a spectral curve of the extinction cross-section of particles is very strongly dependent on particle size. The window disappears for very large or very small particles.

Our results for ice fogs are self-consistant and in general agreement with those of Blau, et al. (Ref. 3). Thus, we can conclude that the indices of refraction tabulated by Irvine and Pollack (Ref. 9) for ice are in error near 2.8 μ.

Techniques involving simultaneous measurements at two wavelengths have been shown to be very powerful. They can provide information that single-wavelength measurements cannot provide on such things as particle-size distributions, the influence of irregular shapes, and the real and imaginary parts of the index of refraction.

SECTION 6

REFERENCES

1. Arnulf, A., Bricard, J., Cure, E., and Veret, C., J. Opt. Soc. Am. 47, 1957, p491.

2. Farmer, C. B., Proceedings of Infrared Information Symposium, 6, No. 1, 1961, p145.

3. Blau, H. H., Jr. and Espinola, R. P., Appl. Opt. 7, 1968, p1897.

4. Blau, H. H., Jr., Espinola, R. P., and Reifenstein, E. C., III, Appl. Opt. 5, 1966, p555.

5. Reisman, E., Cumming, G., and Bartky, C., Appl. Opt. 6, 1967, p1969.

6. Johnston, D. R. and Burch, D. E., Appl. Opt. 6, 1967, p1497.

7. Deirmenjian, D.: Electromagnetic Scattering on Spherical Polydispersions. American Elsevier Publishing, Inc., 1969.

8. Deirmenjian, D., Appl. Opt. 3, 1964, p187.

9. Irvine, W. M. and Pollack, J. B., ICARUS 8, 1968, p324.

10. Plass, G. N., Appl. Opt. 5, 1966, p279.

11. Kattawar, G. W. and Plass, G. N., Appl. Opt. 6, 1967, p1377.

12. Kattawar, G. W. and Plass, G. N., Appl. Opt. 6, 1967, p1549.

13. Mason, B. J.: The Physics of Clouds. Oxford at the Clarendon Press, 1957.

14. Zuev, V. E.; Koshelev, B. P.; Tvorogov, S. D. and Khmelevtsov, S. S., Attenuation of Visible and Infrared Radiation by Artificial Water Fogs, Atmospheric and Oceanic Physics Series, Vol. 1, No. 5, 1965, pp509-516.

15. Ranz, W. E. and Wong, J. B., Ind. Eng. Chem. 44, 1952, p1375.

16. Odencrantz, F. K. and Hildebrand, F. H., Growth and Morphology of Ice Crystals, Naval Weapons Center, China Lake, California.

APPENDIX A

ATTENUATION OF SOLAR RADIATION BY NATURAL CLOUDS

The purpose of this study has been to provide experimental data on natural cloud transmission and on ratios of the extinction coefficients at various wavelengths in the visible and infrared. Specificially, the wavelengths of interest for this experiment have been 0.633, 1.06, 1.6, 2.2, 8.8, 10.6, 12.0, and 13.0 μ. Because of molecular absorption in the atmosphere, the wavelengths were selected in the atmospheric windows.

The initial experiments simultaneously monitored the cloud transmissions at 0.633 and 1.06 μ. The equipment was then modified so that 0.633 μ and 10.6 μ data were monitored continuously while a third channel monitored either 8.8, 12, or 13 μ data. Late in the year, another modification to the equipment allowed the monitoring of either 1.6 or 2.2 μ data, along with the continuous monitoring of 0.633 μ data.

Figure A-1 schematically shows the optical arrangement. A two-mirror coelostat continuously tracks the sun, which is the radiation source. Mirror M1 with a 50 cm focal length and a speed of F/17 forms an image of the solar disk and the clouds in front of the sun onto an aperture stop. The diameter of the solar disk image is 4.37 mm while the aperture diameter used for monitoring cloud transmission is 1.5 mm. An alternate aperture with a diameter of 0.25 mm was used in scanning across the solar disk to check for the effects of near-forward scattering by the clouds. After passing through the aperture, the visible light is separated from the beam by a long-pass beam splitter B1 and filtered with a 50 angstrom half-width interference filter centered at 0.633 μ. A photomultiplier detects this light.

The aperture stop is imaged by mirror M2 onto the entrance slit of a spectrometer which isolates and detects any wavelength of interest in the infrared. A second beam splitter B2 consisting of a germanium flat is employed along with the bandpass filter F2 to isolate 10.6 μ radiation

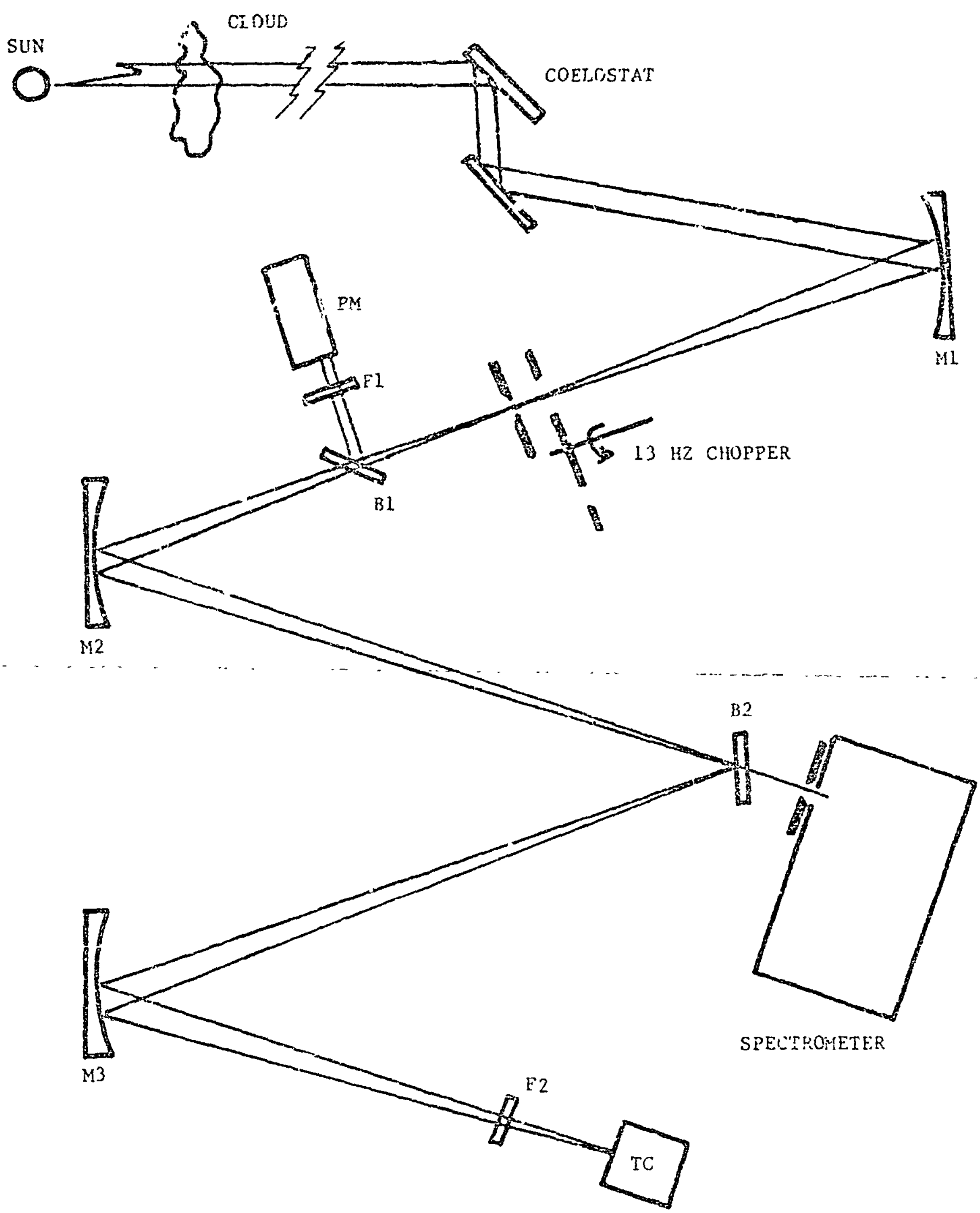

FIG. A-1. Optical diagram of apparatus used to study attenuation by natural clouds.

which is detected by a thermocouple. Mirrors M2 and M3 image the aperture stop on the sensitive area of the thermocouple. The radiation is chopped at 13 cycles.

The detector outputs of the three channels are amplified by phase-locked amplifiers and recorded in parallel on strip-chart recorders. To simplify the data reduction, the chart drives of the recorders are slaved together and time marks are frequently placed on the chart paper. The data are recorded in the form of relative radiant intensity at the aperture stop for the various wavelengths as a function of time. In most cases the clouds were broken so that the detector signal corresponding to clear sky could be determined every few minutes. When the sky was not completely clear between the clouds, the measurement represents the transmittances of the cloud relative to the spot assumed to be clear, rather than the true transmittance. We are concerned primarily with ratios of attenuation coefficients; errors in the ratios produced by thin clouds in the regions assumed to be cloudless are much less than the errors in the attenuation coefficients. Early in the A.M. and late in the P.M. the length of the light path through the atmosphere changes rapidly with time causing changes in the detector signal corresponding to a cloudless sky. This change must be accounted for in order to avoid sizeable errors in positioning the 100% transmittance curve.

Most of the transmission data collected were for cirrus clouds at elevations between 7,000 and 10,000 m, altocumulus and altostratus clouds between about 3,000 and 7,000 m, and dissipating stratocumulus clouds with base heights of about 350 m.

Interpretation and Analysis of Data.--The transmittance, T_λ, at wavelength λ, of a cloud is defined as the ratio of the recorder deflection at the time of interest to the deflection when no clouds are in the line-of-sight between the sun and the instrument. For the sake of discussion let us assume that no scattered energy is detected so that we observe only the unattenuated portion of the original beam. The attenuation may be due to either scattering or absorption. As in previous sections, γ is the average extinction coefficient per unit path length in the cloud of thickness z. Then

$$T_\lambda = \exp(-\gamma_\lambda z), \qquad \text{or} \qquad -\ln T_\lambda = \gamma_\lambda z. \tag{A-1}$$

We are concerned primarily with the ratios of attenuation coefficients, $(\gamma_{\lambda_1}/\gamma_{\lambda_2})$, at different wavelengths which are observed simultaneously so that $z_1 = z_2$. Therefore,

$$(\gamma_{\lambda_1}/\gamma_{\lambda_2}) = (-\ln T_{\lambda_1})/(-\ln T_{\lambda_2}). \tag{A-2}$$

The ratio $(\gamma_{\lambda_1}/\gamma_{\lambda_2})$ is equal to $(\sigma_{ext,\lambda_1}/\sigma_{ext,\lambda_2})$, the ratio used in previous sections. We expect the ratio $(\gamma_{\lambda_1}/\gamma_{\lambda_2})$ for any two wavelengths to vary with the size distribution of the particles and with their composition and shape. Water droplets are probably spherical, while ice particles in cirrus clouds may have a variety of shapes.

If the sun were a point source and the aperture on which the solar image is focussed subtended a sufficiently small angle, no scattered energy would reach the detector, as assumed above. However, since both the sun and the aperture subtend finite angles, a certain amount of scattered energy is detected. For clouds of optical thickness (γz) less than 3 or 4, the scattered energy that is detected is probably singly scattered in the near-forward direction. The fraction that is forward scattered varies with wavelength and particle size so that errors may be introduced by assuming that the ratio of the extinction coefficients can be found by Eq. (A-2). The size of the errors probably could be estimated by use of Mie theory or Monte Carlo methods, but this is beyond the scope of the present project. In the following discussion, we have assumed that Eq. (A-2) is valid. Values of γ_λ and $\gamma_{\lambda_1}/\gamma_{\lambda_2}$ should be regarded as apparent values because of possible errors due to near-forward scattering.

The recorded data on incident intensity as a function of time were digitized and operated on by a computer to yield tables of the instantaneous transmittance T_λ, and $-\ln T_\lambda$, along with the cumulative integral of $-\ln T_\lambda$ as a function of time for a given cloud. These tables were examined and the data were grouped into four intervals as a function of $-\ln T_{0.63}$, so that each group represented different optical thicknesses. The values of $-\ln T_{0.63}$ defining the individual groups were 0.1 to 0.5, 0.5 to 1, 1 to 2, and 2 to 5. Values less than 0.1 and greater than 5 were excluded because of potentially large errors due to errors in drawing in the 100% transmission curve and the zero-transmission curve, respectively. Once the data were grouped, the computer was employed again to give tables of the ratios of the attenuation coefficients at the various wavelengths. Also tabulated was the average $(-\ln T_\lambda)$ for each interval.

At the present time, the data analysis is complete for a group of clouds which were monitored simultaneously at 0.633, 10.6, and 13 μ, for another group studied at 0.633 and 1.06 μ, and for a third group studied at 0.633 and 10.6 μ. The results are summarized in Table A-1. Typical average values are given for the type of cloud indicated. Variations occur with changing particle-size distribution. The mean standard deviations are also shown in Table A-1, along with the mean values for the data obtained during this phase of this company-sponsored program.

Qualitative explanations of most of the results can be given on the basis of Mie theory and available information about typical particle sizes and the indices of refraction of ice and water. A dissipating stratocumulus cloud undoubtedly consists of smaller particles than a relatively stable cumulus cloud. If the particle radii are much smaller than 10 μ, the extinction coefficient at 10.6 μ is expected to be much less than at 0.633μ, aside from any differences in the indices of refraction. This probably accounts for the small ratio (0.23) of $\gamma_{10.6}/\gamma_{0.63}$ observed for a dissipating stratocumulus cloud. Somewhat larger values of this ratio were observed for two other water clouds whose particles were probably larger than those in the dissipating cloud. Because of the large ratio (10.6:0.633) of the wavelengths involved, the ratio $\gamma_{10.6}/\gamma_{0.63}$ is expected to be sensitive to particle-size distribution, particularly if the particles are much smaller than the longer wavelength.

In relatively stable clouds, $\gamma_{10.6}/\gamma_{0.63}$ seemed to have little correlation with $-\ln T_{0.63}$. This implies that the particle-size distribution remained relatively stable and that the recorded large variations in $-\ln T_{0.63}$ (from 0.1 to 5 was not unusual) were due to changes in cloud thickness or particle density, or both. Since multiple scattering is greater in thick clouds than in thin ones, this result also implies that the amount of multiply-scattered radiation is negligible. For the water clouds which were obviously dissipating $\gamma_{10.6}/\gamma_{0.63}$ decreased with time, indicating a decrease in the sizes of the particles due to evaporation.

Another interesting result is the wide variation in $\gamma_{13}/\gamma_{10.6}$ which was observed for water clouds. Since the ratio of the wavelengths is approximately unity, we would not expect $\gamma_{13}/\gamma_{10.6}$ to be sensitive to changes in particle sizes except for changes produced by differences in the indices of refraction at the two wavelengths. If the particle sizes were a few times greater than either wavelength, the attenuation would be relatively independent of changes in wavelength between 10.6 and 13 μ. If the particles were much smaller than λ, and if the indices were similar at both wavelengths, $\gamma_{13}/\gamma_{10.6}$ would be less than unity. Therefore, the large (2.05) value of this ratio observed for the small particles in the dissipating stratocumulus cloud must result from differences in the indices of refraction at the two wavelengths.

Values of n_r and n_i tabulated by Irvine and Pollack (Ref. 9) are presented in Table A-2 for the wavelengths of interest in this study; they provide the basis of an explanation for the wide variations and for the unusually large values of $\gamma_{13}/\gamma_{10.6}$. It should be borne in mind that the tabulated values of n_r and n_i are subject to sizeable errors because of the experimental difficulties in measuring these quantities. However, the accuracy is probably adequate for the following qualitative discussion.

The small increase in n_r from 1.18 to 1.22 between 10.6 and 13 μ cannot account for the large increase in γ. Therefore, the increase in

γ must result from the increase in n_i which is approximately a factor of 4. Mie theory shows that the influence of absorption becomes increasingly important as r decreases; in the limit of decreasing r, γ is independent of n_r and is proportional to n_i. From theoretical curves presented by Kattawar and Plass (Ref. 11), we can show that σ_{ext} at 13 μ is largely due to σ_{abs} and that σ_{abs} is nearly proportional to n_i for particles smaller than 1-2 microns. The agreement between this theoretical result and our experimental results further substantiate our assumption that the dissipating stratocumulus clouds consist of smaller particles than the more stable clouds.

The ratio $\gamma_{13}/\gamma_{10.6}$ for ice clouds is always greater than unity but considerably less than for water clouds. The ratio $n_{i,13}/n_{i,10.6}$ is only about 1.6 for ice, while it is 3.8 for water. However, the increase in n_r in going from 10.6 to 13 μ is much greater for ice than for water. Theoretical curves by Plass (Ref. 10) show that σ_{ext} is only slightly dependent on n_r and n_i in the 10-13 micron region for particles larger than approximately 20 microns. The ice particles are probably large enough that the differences in the indices have a small influence so that $\gamma_{13}/\gamma_{10.6}$ is approximately one.

One of the more surprising results came from the cirrus (ice) clouds for which $\gamma_{10.6}/\gamma_{0.63}$ was always significantly greater than unity. By contrast, this ratio was always less than one for water clouds. On a few occasions a layer of broken ice clouds occurred above a layer of broken water clouds. By comparing the recorder tracings, it was easy to determine which type of cloud was passing into the line-of-sight. From Table A-2 we see that the indices are nearly the same for ice as for water at both wavelengths. If this is true, the difference in the ratios of extinction coefficients must be due to either the irregular shapes of ice particles or to their larger size.

Results of the near-forward scattering measurements on artificial ice clouds reported in Section 3 indicate that Mie theory is at least approximately correct for ice particles. Of course, the ice particles in natural clouds are probably much larger than in the artificial clouds. The scattering by the larger particles might deviate more from Mie theory. Near-forward scattered radiation which reaches the detector undoubtedly contributes to the large ratio for ice. Since the forward scattering increases with r/λ, more scattered energy at 0.633 μ than at 10.6 μ, this causes the apparent extinction to be less than it actually is at the shorter wavelength.

The value of $\gamma_{10.6}/\gamma_{0.63}$ for the artificial ice fogs is seen from Table A-1 to be 0.40, which is much less than for the natural ice clouds. No scattered light was detected in the measurements on artificial clouds, but the big difference is probably due to differences in the particle sizes. The ratio for the same wavelengths for the artificial water fogs in the present study is also smaller than for the altocumulus. Again, this is probably due to larger particles in the altocumulus. The value for the artificial fogs is typical of dissipating stratocumulus.

We have measured the relative intensity at 0.633 μ as we scanned across the solar disk with different types of clouds in the path. From these results, which have not been reduced yet, we hope to obtain information on the scattering at small angles. Monte Carlo techniques will also be used to estimate the errors in our measurements of the ratio of extinction coefficients due to the detection of forward-scattered radiation. It is probable that the errors are unimportant except for ratios involving 0.633μ and another wavelength considerably longer.

The particles in the water and ice clouds studied at 0.633 and 1.06 μ were probably larger than the wavelength of the light so that the attenuation was relatively independent of wavelength. Thus the ratio of extinction coefficients was close to unity. Dissipating clouds with smaller particles might attenuate less at 1.06 μ than at 0.633 μ.

The results for artificial water fogs can be compared with previous work in this laboratory by Johnston and Burch (Ref. 6). The wavelengths studied previously were slightly different, but they are sufficiently close for comparison. Temperatures of the fogs generated by Johnston and Burch were higher so that a greater percentage of large particles were probably present. This is reflected in the ratio $\gamma_{10.0}/\gamma_{0.54}$, which is sensitive to the number of large particles. The smaller (1.2) value of $\gamma_{13.5}/\gamma_{10.0}$ is also indicative of larger particles.

TABLE A-1

SUMMARY OF APPARENT EXTINCTION COEFFICIENT RATIOS
FOR NATURAL CLOUDS AND COMPARISON WITH ARTIFICIAL CLOUDS*

Type of Cloud or Fog	$\frac{\gamma_{1.06}}{\gamma_{0.63}}$	$\frac{\gamma_{10.6}}{\gamma_{0.63}}$	$\frac{\gamma_{13}}{\gamma_{10.6}}$
	Natural Clouds		
Water, Dissipating Stratocumulus @ 350 m		0.23 (0.06)	2.05 (0.19)
Water, Altocumulus @ 3100 m		0.49 (0.18)	1.63 (0.13)
Ice, Cirrostratus @ 7300 m		1.38 (0.10)	1.10 (0.04)
Ice, Cirrus @ 7600 m		1.29 (0.12)	1.13 (0.04)
Ice, Cirrus (heights unknown)	1.03 (0.03)		
Water, Cumulus (heights unknown)	1.02 (0.04)		
	Artificial Fogs		
Water (Present Study)		0.24	
Ice (Present Study)		0.40	
Water (Johnston and Burch)	$\gamma_{1.01}/\gamma_{0.55}$ = 1.08	$\gamma_{10.0}/\gamma_{0.55}$ = 0.54	$\gamma_{13.5}/\gamma_{10.0}$ = 1.2

*The mean standard deviation is shown in parenthesis for the natural cloud data.

TABLE A-2

REAL AND IMAGINARY PARTS OF INDEX OF REFRACTION[a]

λ (microns)	Water		Ice	
	n_r	n_i	n_r	n_i
0.54	1.334	1.3×10^{-9}		
0.63	1.331	1.0×10^{-8}		
1.01	1.326	2.4×10^{-6}	1.302	2.3×10^{-6}
1.06	1.325	1.07×10^{-6}	1.301	2.3×10^{-6}
10.0	1.21	0.053	1.15	0.041
10.6	1.18	0.076	1.21	0.067
13.0	1.22	0.292	1.61	0.11
13.5	1.25	0.320	1.61	0.09

[a] Values are from Irvine and Pollack (Ref. 9).